

AD-A043 158

MINISTRY OF DEFENCE LONDON (ENGLAND) DIRECTORATE OF --ETC F/G 20/4  
HIGH SPEED LIQUID IMPACT STUDIES, (U)  
DEC 76 J E FIELD, J J CAMUS, D A GORHAM

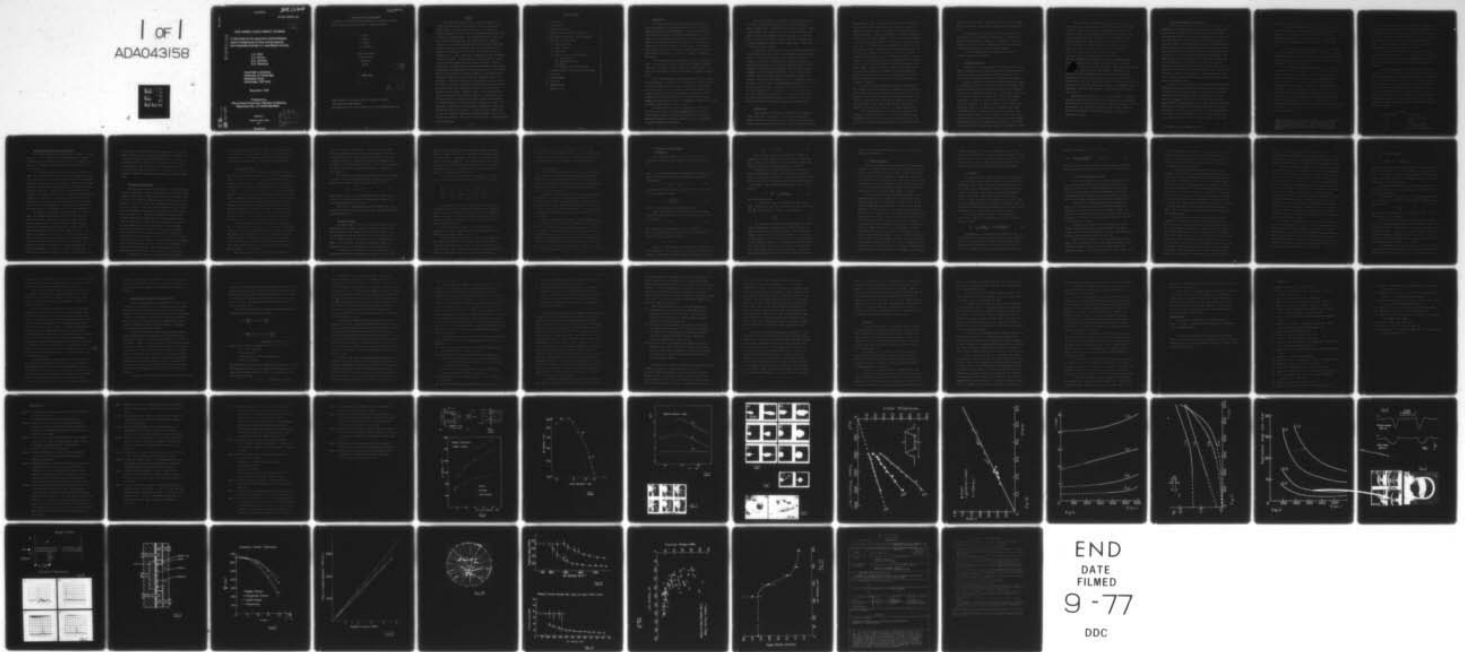
UNCLASSIFIED

DR-MAT-203

DRIC-BR-55079

NL

1 of 1  
ADA043158



UNLIMITED

BR 55079

DR MAT REPORT 203

*Law*

BR-55079

## HIGH SPEED LIQUID IMPACT STUDIES

AD A 043158

A discussion of the apparatus and techniques used in studying liquid drop and jet impacts and assessing damage in a quantitative manner

J.E. Field  
J.J. Camus  
D.A. Gorham  
D.G. Rickerby

Cavendish Laboratory  
University of Cambridge  
Madingley Road  
Cambridge CB3 0HE

December 1976

Prepared for  
Procurement Executive, Ministry of Defence  
Agreement No. AT/2029/066/MAT

AD No. \_\_\_\_\_  
DDC FILE COPY,

COPYRIGHT ©

CONTROLLER HMSO LONDON  
1976

UNLIMITED

DDC  
RECEIVED  
AUG 18 1977  
*A*

14

6

HIGH SPEED LIQUID IMPACT STUDIES

A discussion of the apparatus and techniques used in studying liquid drop and jet impacts and assessing damage in a quantitative manner.

10

J E Field,  
J J Camus,  
D A Gorham,  
D G Rickerby.

Cavendish Laboratory,  
Madingley Road,  
Cambridge,  
CB3 0HE.

18

DRIC

19

BR-55079

11

December 1976

12

64p.

APPROVED BY	
NTS	Waste Section <input checked="" type="checkbox"/>
UNC	Box Section <input type="checkbox"/>
UNCLASSIFIED	<input type="checkbox"/>
CLASSIFICATION	
DISTRIBUTION AVAILABILITY CODES	
Dist.	AVAIL. and/or SPECIAL
A	

407 962-

Report prepared for Procurement Executive, Ministry of Defence  
under Agreement AT/2029/066/MAT  
Work monitored by Dr N S Corney Mat R7 and Mr A A Fyall Materials Dept, RAE

64p.

## ABSTRACT

This report summarises the results of a broad programme of work on high speed liquid impact. Two methods were used for producing high velocity impact. The first involved projecting a jet of liquid at a stationary target while in the second 25.4 mm diameter specimens were fired by a gas gun at suspended drops. One of the main objectives of the study was to place the jet method on a sound quantitative basis. Detailed studies of jets, using high speed photography at microsecond framing rates, allowed the conditions for producing stable and reproducible jets to be obtained for a wide range of jet velocities (up to  $1000 \text{ m s}^{-1}$ ) and jet diameters (0.4 to 3.2 mm). Information on chamber design and jet parameters is given in the report. The next aspect of the study involved an attempt to relate jet impact damage with that caused by drop impact. This was achieved after experiments in which high speed photography, pressure measuring techniques and damage studies all played important roles. The establishment of the jet method as a quantitative approach to liquid impact studies has practical application since the method has advantages in its ease of operation, its ability to simulate very large drop sizes, and the fact that the target is stationary. High-speed photography and pressure measurements with 250  $\mu\text{m}$  diameter PZT4 transducers were used to study the pressures generated by liquid impact. Evidence was found of high edge pressures in an annular region around the main water hammer area. The final section of the report describes a hydrostatic test apparatus developed for measuring the "residual strength" of brittle specimens following liquid impact. The importance of quantitatively assessing damage is emphasized in this report. With brittle solids such as glasses it is shown that large strength losses can take place before the damage reaches visible dimensions. This clearly has practical importance. The factors affecting the shape of residual strength curves are discussed.

Table of Contents

1. Introduction	1
2. Jet Production	2
3. Chamber Characteristics	4
4. High-speed Photography of Jet Behaviour	6
5. Recording with Photocells; Spark Photography	9
6. Relating Jet and Drop Impact	10
(a) Impact with Drops	11
(b) Liquid Jet Impact	12
(c) Crater Shape	14
(d) Pressures Produced by Liquid Impact	15
(i) Introduction	15
(ii) High Edge Pressures	17
(iii) Region c	18
(iv) Pressure Transducer Measurements	19
7. Residual Strength of Glass After Liquid Jet Impact	24
8. Conclusions	31
9. Acknowledgements	34
10. References	35
11. Figure Captions	37
<b>Figures 1 - 25</b>	

1. Introduction

It is well known that the impact of a liquid and a solid has important consequences in the rain erosion of aircraft, the erosion of steam turbines and in cavitation phenomena. The work described in this final report was primarily concerned with the damage produced by the impact of large water drops. This kind of work is important since it is known that a large mass of liquid in a single drop can cause much more damage than the same mass divided into smaller drops. Thus although a rain field may contain only a relatively few large drops, it can be these which determine the catastrophic failure of a component, for example, a glass radome.

We used two methods for simulating the collision with large water drops. The first was the technique first devised by Bowden and Brunton (1958, 1961) for projecting a jet of liquid at a stationary target. The second was a gas gun which can fire 25.4mm diameter specimens at stationary drops.

Both of these methods have their own advantages. The first method has the disadvantage of shooting a jet of liquid but has distinct advantages in its ease of operation, low construction cost, and the velocity range that can be covered. The second is nearer the practical situation, since a spherical drop is struck, but has disadvantages as regards the size of specimen which can be projected and the deceleration (without further damage) of the specimen after impact. The suspension of spherical water drops of diameter greater than 2mm is also a problem.

One of the objectives of the present project was to see if the jet method could be put on a sounder quantitative basis. This has involved extensive studies of jet production and impact (aided greatly by high-speed photography at microsecond framing rates) and the measurement of pressures produced by liquid impact.

We have also attempted to put damage assessment on a more quantitative basis. This has involved measuring the "residual strengths" of samples following impact. Strength was measured using a hydraulic strength testing technique. As is shown later curves of residual strength versus impact velocity (for a constant jet size) show a sharp fall of strength when a critical velocity region is reached. This loss of strength comes at velocities below those which give visual impact damage. Clearly this is a point of practical interest.

As will become clear later, one of the conclusions from the research is that reproducible, stable jets can be produced which can simulate drop impact. For this reason the report includes experimental details and references so that any of our apparatus can be readily reproduced. For example there will be details of (i) the jet production method, (ii) the gas gun, (iii) the hydraulic strength tester, and (iv) pressure measuring techniques. All of the above are relatively "low cost" items which any laboratory with a well-equipped workshop and electronics section could construct. We have also used high-speed cameras extensively and these are expensive items. However, although high-speed framing photography giving several sequential pictures was essential for our work in which we had to establish conditions of jet stability etc. it was not so necessary for future workers using the jet method. A section is included therefore describing how spark photography and photo-cell methods could be used to observe jet shapes and velocities in a simple and inexpensive manner.

## 2. Jet Production

The basic method for jet production was worked out by Bowden and Brunton (1958, 1961). A projectile is fired into a stainless steel chamber containing a small quantity of water sealed in by a neoprene disc. The projectile and neoprene drive forward as a piston and extrude the water

through a narrow orifice. The ratio of water jet velocity to projectile velocity is typically 3-5 times (see later for details). Figure 1(a) shows schematically the design of the stainless steel chambers which we found most suitable. A range of jet diameters is obtained by varying the dimension  $d$ . In preparing a chamber the inner contours should be smoothed so that there are no sharp changes. A few firings are usually needed for a new chamber to "run in", but then the chamber behaves reproducibly for many hundreds of shots. The neoprene discs are usually punched out from 2mm thick sheet (the punch is a slotted steel block with a vertical cylindrical hole down which a rod of 4.8mm diameter is pushed). The back surface of the disc should be flush with the rear surface of the chamber. A convenient way to load the chamber is through the nozzle using a hypodermic syringe. Care has to be taken to ensure that the chamber liquid does not contain particles or air bubbles. The liquid/air interface affects the jet production but this is discussed in detail later, where specific loading instructions are given for stable jet production for a variety of diameters.

Various other chamber designs were tried but this proved the most suitable for present requirements. The chamber is not optimised for producing high jet velocity to projectile velocity ratios, since our jets adequately cover the range required in rain erosion applications. If the application had been to produce high velocity liquid jets for mining or rock cutting more suitable chamber design could give jet velocity to projectile ratios of 10 to 12 times (see, for example, Rhyning 1973).

In the original apparatus a commercial spring operated air gun was used to fire the lead projectile. This basic arrangement has now been modified and the lead slugs propelled by compressed gas. The compressed gas is typically nitrogen but helium is useful for high-velocity

work (see below for details). The gas bottle is used to load a chamber with gas, and the gun is then fired by triggering a fast-acting solenoid valve.

A problem which we had at the start of this particular project was obtaining jet velocities below a few hundred  $\text{ms}^{-1}$ . (There were no problems in obtaining higher values up to a few  $1000 \text{ms}^{-1}$ ). This was eventually overcome by using the arrangement illustrated in figure 1(b); the added piston effectively acts as a momentum exchanger.

It is worth emphasizing at this stage the low cost of the apparatus required for jet production.

### 3. Chamber Characteristics

Chambers with jet orifice diameter,  $d$ , in the range 0.4 to 3.2 mm have now been fully tested. Calibration curves have also been obtained of jet velocity versus gas gun pressure for all the various values of  $d$ . A typical set of calibration curves for  $d = 0.8 \text{ mm}$  is shown in figure 2.

Figure 3 shows the variation of jet velocity with orifice diameter at a constant slug velocity of  $175 \text{ms}^{-1}$ . The axes are logarithmic, and it can be seen that the points fall into three regions, in two of which the  $V/d$  curve can be approximated by power laws. For the larger nozzles, with  $d$  from 2 mm to 3.2 mm, the jet velocity  $V_j \propto d^{-0.88}$ . An intermediate range from  $d = 2.0 \text{ mm}$  to  $1.0 \text{ mm}$  is defined by the relationship  $V_j \propto d^{-0.44}$ , and this is the range over which the jets are found to be most stable (figure 3). The third region is suggested by the single (confirmed) result of the smallest nozzle (0.4 mm) which gives a lower velocity than the 0.8 mm one. This is thought to be due to the increase in viscous effects in the extremely small orifice, which reduces chamber efficiency very sharply. Any turbulence at the entrance to the orifice section will also become increasingly important as the diameter is reduced.

The variation in the conversion ratio, i.e. the value of  $V_j/V_s$  ( $V_j$  = velocity,  $V_s$  = slug velocity) is given in figure 4 for three chamber sizes (all loaded to position F with convex outwards liquid/air interfaces). The ratio is not constant throughout this velocity range for the smaller diameters, but in the larger ones it is approximately constant. When the chambers were loaded to position E the velocity ratios were increased by about 7.5% for the 0.8 mm nozzle and about 5% for the 1.6 and 2.4 mm nozzles. Obviously a number of effects are occurring which lead to these complex results. The peaking of the  $V_j/V_s$  curves for the 0.8 mm and 1.6 mm nozzles indicates that there are mechanisms for reducing the conversion efficiency which become more effective both for high velocities and for low velocities. The velocity limit of  $V_j/V_s$ , i.e. the ratio of chamber area to nozzle area, is 10 for the 0.8mm and 9 for the 1.6mm diameters. Therefore, all the hydrodynamic effects considerably reduce the efficiency of the nozzle. These become less important as the ratio of  $V_j/V_s$  decreases, i.e. as the orifice diameter increases. The  $V_j/V_s$  curve for the 2.4mm nozzle is very flat, and not far below the theoretical maximum of about 4. This suggests that the hydrodynamic conditions within the chamber are becoming much more complex as 'd' is reduced.

The detailed shape of the above curves is quite complex. As described in previous reports we have had some success in predicting nozzle performance by extending the theory of Rhyning (1973), which was for an exponential nozzle. The main point from the practical viewpoint is that for given conditions the jets have reproducible velocity and form. (More is said about jet characteristics below).

4. High-speed Photography of Jet Behaviour

High-speed photography has been used extensively in our work. Early photographic work on impact in this laboratory was with a Cranz-Schardin system (Bowden and Brunton, 1961), a Beckman and Whitley (model 189) rotating mirror camera (Bowden and Brunton 1961, Brunton 1961, Bowden and Field 1964, and Brunton and Camus 1970), and a Beckman and Whitley 501 single-frame image converter camera (Camus 1971). All these systems have drawbacks which limit their usefulness for this application. Our Cranz-Schardin system provides very high resolution over a limited area, but it is difficult to set up and successive frames suffer from parallax. The Beckman and Whitley 189 rotating mirror camera also has good resolution and a high framing rate. However, liquid jet production cannot be triggered on a microsecond scale and so with a rotating mirror camera of limited access (film over only part of the cycle) the success rate is low. The Beckman and Whitley image converter is a single frame camera, and to obtain a sequence involves several cameras, with the inherent problems of light loss or parallax errors.

The camera which has recently been adopted for this work, the Imacon<sup>\*</sup> framing image converter, overcomes these disadvantages, at the expense of a slightly inferior resolution capacity. It has three basic advantages over the other high-speed photographic systems available: (i) it is synchronisable from the event, (ii) it is sensitive enough to record scattered light from opaque objects, using conventional light sources, and (iii) the use of 'Polaroid' film facilitates large numbers of sequences being taken, thus improving calibration data and allowing reproducibility of the water jets to be investigated. It is also a movable camera which can be taken to the event; this is a tremendous advantage for a camera

\* J. Hadland P.I. Ltd., Bovingdon, Herts, U.K.

(the Imacon weighs 35 kg, an A.W.R.E. C4 camera 2000 kg ! )

The camera was triggered by detecting, with a photomultiplier, reflected laser light from the water jet. The signal from the photomultiplier was fed through suitable delay units to the Xenon flash light source and the camera. The single flash pictures used the same synchronisation arrangement, and were illuminated by a 150 ns spark source.

An Imacon sequence, using shadowgraph photography, of a  $750 \text{ ms}^{-1}$  jet impacting a PMMA block is shown in figure 5. Such pictures can give information about the jet velocity and head profile, associated air shocks, the sideways flow of liquid after impact, the various stress waves in the target block and the growth of damage.

Figure 6 illustrates the kind of data which can be obtained about jet stability (only 2 frames from each sequence are given). The figure gives information for three chamber sizes, and in each case for both empty and full loading of the exit portion of the chamber (positions E and F of figure 1a). In all examples a central 'core' of liquid is surrounded by a 'bag' of spray; this spray has a negligible effect on the damage. For liquid impact erosion studies the jets of 6(a), (c), (d) and (f) would be suitable provided the specimens were within 10 mm of the nozzle. The jet in (b) emerges with a hydrodynamic instability and this is rapidly magnified by the air drag. However, even if a jet is initially stable aerodynamic forces can eventually cause Taylor instability\* to develop. For jets of a few  $100 \text{ ms}^{-1}$  this takes place a few centimeters from the nozzle plane.

\* When a jet (or drop) is acted on by aerodynamic forces a stage can be reached when these forces exceed the restoring forces of the liquid's surface tension. Taylor instability is when the deformation to the liquid surface causes unstable surface waves to develop which grow exponentially with time (Taylor 1950, Harper et al 1972, Simpkins and Bales 1972).

In figure 6(e) a precursor jet has formed; with an empty end section (position E in figure 1) of the larger orifice chambers this took place whether the liquid/air interface was convex or concave. With a full chamber a precursor or Munroe jet developed only when the liquid/air interface was concave inwards (figure 7). The production of the precursor jet can be explained in similar terms to that of a jet from a shaped-charge (see, for example, Birkhoff et al 1948).

The use of single-shot photography is illustrated in figure 8. In 8(a) ablation from the head of the jet forms the 'bag' of spray; note that it is possible to make out the central high-density core of liquid. 8(b) shows a later stage with another jet which has developed Taylor instability.

In cases where hydrodynamic or aerodynamic instability modes develop the jets are not suitable for erosion studies. However, we now understand reasonably well the conditions which produce these instabilities. Jets in figure 6 which would be suitable for erosion studies would be those illustrated in 6(a), (c), (d) and (f) at a stand-off distance of ca. 10 mm. The bag of spray which develops has been shown to be made up of micron sized drops and these do not contribute to the damage. The jets have a rounded nose. This can be counted as an advantage since it makes simulation of impact with a rain drop more realistic. Table 1 summarizes the loading conditions required for reproducible, stable jets of various diameters.

Table 1

Nozzle diameter/mm	Liquid Interface
0.4	Position E (see figure 1)
0.8	Position E
1.6	Position E or position F, convex outwards
2.4	Position F, convex outwards

### 5. Recording with Photocells; Spark Photography

We have used high-speed framing photography extensively. The question arises as to how important such camera equipment is for anyone constructing our jet apparatus and wanting to make erosion studies. The answer is that although a camera like the Imacon would be beneficial it is not essential.

The slug (projectile) velocity can be measured very simply in a number of ways of which probably the simplest is to interrupt light beams falling on photocells spaced at measured distances apart. Once projectile velocities are known and the gun is calibrated in terms of firing pressure, stable jets of various sizes and velocities can be obtained, following the instructions given above. The ratios of  $V_J/V_S$  discussed earlier could then be used to calculate the jet velocities. Comparison of damage sites on PMMA, glass, aluminium etc. illustrated in this report and in other listed publications could be used to confirm that all was well. However, with very little further expenditure it would be possible to measure the jet velocity directly, again using photocells or 'spark' photography.

Using sparks to obtain short exposure photographs is relatively simple. As a high-speed photographic method it was first used by Fox Talbot in the 1850's; apparatus is now available commercially for producing intense sparks at rates up to  $\sim 10^5$  Hz. A simple spark gap (condensers discharged between electrodes) has a duration of  $\sim 10^{-5}$  s. With high melting point electrodes and small gaps durations for 'free' sparks can be reduced to less than  $10^{-6}$  s. This kind of exposure time is perfectly adequate to give sharp jet pictures. Two spark gaps triggered with a delay would give two displaced images on a single plate. This would allow jet velocity and shape to be recorded photographically. This system is recommended. If the spark is not bright enough there are various ways of increasing its energy: (i) use of a sliding spark - this

helps because it increases the spark length and because it also increases spark resistance and uses the condenser energy much more efficiently (for a practical arrangement see Luy and Schade 1956); (ii) use of a gas such as argon blown over the spark gap; (iii) a cell built around the gap so that high pressure argon can be used. All of these modifications can increase the spark output by large factors (2 to 10 times). For a fuller discussion and details of commercial light sources see the book by Früngel (1965).

#### 6. Relating Jet and Drop Impact

This topic was central to the research project. It involved trying to answer two questions. Firstly, can impact with jets give similar damage patterns to those produced by spherical drops? Then if the answer to that was yes, what jet size gives comparable damage to a particular sized drop impacting at the same velocity? The reasons that the answers are not easy to settle are varied. In the first place, the impact of a perfect cylinder gives a 'water hammer' pressure over the full impact area of the cylinder, while a drop only gives a 'water hammer' pressure over a small central area which depends on drop radius and impact pressure (Bowden and Field 1964). Secondly there is evidence that high edge pressures exist around the 'water hammer' pressure area (observations on this have been made during the time of the present contract both by other workers and by us (see later)). Thirdly, there is the fact that perfect cylinders with radius equal to the orifice diameter are not easy to produce. The reasons for this are discussed in detail below. It means that the jets we recommend using have at the 'stand-off' distance of 10 mm a head diameter which is larger than the orifice diameter. This head diameter depends on the chamber loading and jet velocity. Data are given for 4 jet sizes later.

Our approach was a multiple one: (i) we made detailed studies of

the damage produced by both jet and drop impact on aluminium, PMMA and glass targets; (ii) we photographed the impact of jets and drops, and in the particular cases of transparent targets and 2-D drops we observed stress wave propagation in them; (iii) pressure records were taken.

(a) Impact with Drops

In the early stages of this work drop impact damage was studied by examining specimens kindly provided by A.A. Fyall of R.A.E. Farnborough. During the last year of the project one of us (David Rickerby) built a gas gun so that we could fire at suspended drops ourselves. This gun has a barrel diameter of 25.4 mm and can fire projectiles up to a velocity of  $\sim 400 \text{ ms}^{-1}$ . It was based on a gun built in this laboratory by Hutchings and Winter (1974) for solid particle erosion studies. Reference to their paper is recommended for anyone wishing to construct such a gun. Basically it consists of a high-pressure chamber (a metal gas bottle), a double diaphragm firing system and a long barrel: velocities are recorded by photocells positioned near the end of the barrel. Suitable electronics have been constructed so that muzzle velocities of the projectiles are displayed directly. It is worth emphasizing that such guns have highly reproducible characteristics and are relatively simple to construct.

Specimens of PMMA and aluminium were mounted in projectiles and fired at suspended drops. The impact process was recorded with the Imacon so that it was possible to measure impact velocity in each case within  $\pm 3\%$ . High magnification photographs were taken of the drop immediately prior to firing the gun. The photographic records allowed accurate values ( $\pm 2\%$ ) of drop size and curvature to be taken. This was important since drops evaporate quite rapidly after suspension, and misleading answers could be produced if firing was delayed.

Water drops of greater than 2-3 mm in diameter are difficult to

suspend. The range of drop sizes was extended up to 6 mm by using a mixture of gelatine and water. Impact 'crater' dimensions were measured by taking Talysurf traces and by microscopic observation. A typical set of results of impact mark dimensions versus velocity for PMMA is shown in figure 9. The insert shows the quantities a, b and c which were measured. Note that they have been plotted non-dimensionally by dividing by the drop diameter  $d'$ .

Note that if the line for  $\frac{c}{d'}$  is extrapolated back it passes through the origin. This point is discussed further in a later section. The equation for this line is given by equation 1, when  $V$  is in  $\text{ms}^{-1}$

$$\frac{c}{d'} = 6.16 \times 10^{-4} V \quad (1)$$

Figure 10 gives a plot of  $c$  versus drop diameter for an impact velocity of  $304 \text{ ms}^{-1}$ . Note that the water and the gelatine/water drops all fall near the same straight line of slope  $\sim 0.2$ .

The increase of damage dimensions with drop diameter and velocity is discussed further in a section devoted to impact pressures and durations caused by liquid impact.

#### (b) Liquid Jet Impact

The damage parameters a, b and c (see insert on figure 9) were also measured for water jet impact. Results were obtained for 0.4, 0.8, 1.6 and 2.4 mm nozzles at the stand-off distance of 10 mm. Nozzles 0.4 and 0.8 were loaded to position E (see figure 1a) and the larger two to position F. Figure 11 shows how  $c$  varies with velocity for damage marks on PMMA for all four nozzles. The results are replotted in figure 12 in dimensionless form (i.e. crater dimension over nozzle diameter,  $d$ ).

If the water jets had maintained the nozzle dimensions up to the 10 mm stand-off then there should have been no change in  $c$  with velocity.

However, as our photographic work has shown, when a chamber is loaded to position F (figure 1a) the jet has a 'mushroom' head (see insert figure 12). This 'head' is a consequence of two effects (i) the liquid in the final section of the chamber (i.e. that between positions E and F) which is pushed aside by the faster moving liquid which has been forced through the tapering section of the chamber, and (ii) air drag which would be expected to be some function of jet velocity.

The measurements can be used to give equations for  $c$  for each nozzle. The four equations are as follows for  $V$  in  $\text{ms}^{-1}$  and  $c$  in mm,

$$\begin{aligned}
 c_{0.4} &= 0.4 + 0 + 4.9 \times 10^{-14} V^{4.63} \\
 c_{0.8} &= 0.8 + 0 + 8.5 \times 10^{-9} V^{2.85} \\
 c_{1.6} &= 1.6 + 0.225 + 1.96 \times 10^{-3} V^{1.00} \\
 c_{2.4} &= 2.4 + 1.65 + 3.8 \times 10^{-7} V^{2.31}
 \end{aligned}
 \tag{2}$$

The first term on the right is the nozzle diameter. The second is a function of the mass of liquid between positions E and F (therefore equal to 0 for the 0.4 and 0.8 nozzles and is obtained by extrapolation back to zero velocity. The final term depends on velocity; the 0.4 mm nozzle has the strongest dependence on velocity particularly above  $450 \text{ ms}^{-1}$  (see figures 11 and 12).

The results plotted in figures 9, 11, 12 (and expressed in equations 1 and 2) can be replotted to give the equivalent drop size in mm that the four chambers produce (figure 13).

One of the objects of the work was to simulate impact with large water drops; this has clearly been achieved. The two large nozzles cover impacts with large masses of water; equivalent drop sizes in the range 10 to 50 mm. The 0.4 mm nozzle is particularly useful for simulating impact with 2 mm diameter drops since the ratio of drop diameter to

orifice diameter is almost exactly constant (i.e. close to 5) for velocities in the range  $300-600 \text{ ms}^{-1}$ . The 0.8 mm nozzle simulates drops of diameter  $\sim 4.5 \text{ mm}$  for a similar range. If 3 mm drops had to be simulated a nozzle with an orifice diameter of 0.6 mm would suffice.

### (c) Crater Shape

Craters have been measured by taking Talysurf traces and by microscopic observation. Earlier work on this project was reported by Dr Gorham in his thesis (Gorham 1974); more recent work (the results for figures 7-10) was obtained by D.G. Rickerby. His work on damage patterns produced by drop impact is still in progress and will be reported in detail in his thesis (end of 1976).

It appears from present results that our jets do produce similar damage patterns to equivalent sized drops. The reason for this is basically that the initial 'water hammer' pressures in both cases controls the amount of damage. Damage extension during the later stages of flow (when the liquid is behaving incompressibly) is relatively small and not significantly different for drop and jet impact in the velocity range we have studied.

Figure 14 shows Talysurf profilometer records from PMMA specimens. The top record (a) is for a jet impact at  $290 \text{ ms}^{-1}$  from a 0.4 mm nozzle. The trace in (b) was taken from a specimen which had impacted an  $\sim 2 \text{ mm}$  drop at  $260 \text{ ms}^{-1}$ . The profile in (b) was taken from one of the series of specimens lent us by Mr A.A. Fyall. In looking at the records it is important to realise that the vertical magnification is 100x that of the horizontal. Although detailed differences can be found it is clear that the jet is able to reproduce the drop damage very accurately. The ratio of drop to nozzle diameter is close to the factor 5 predicted by figure 13.

(d) Pressures Produced by Impact(i) Introduction

When a liquid mass impacts a rigid surface at a velocity  $V$ , a pressure,  $P$ , given by the 'water hammer' equation should be reached, i.e.

$$P = \rho C V \quad (3)$$

where  $\rho$  is the liquid density and  $C$  the appropriate shock velocity in the liquid. For the velocities of interest in the present work  $C$  can be approximated by,

$$C = C_0 (1 + 2 V/C_0) \quad (4)$$

(see Heymann 1969), where  $C_0$  is the sound speed in water. If the target is not rigid, equation 3 becomes

$$P = \frac{\rho C \rho' C' V}{\rho C + \rho' C'} \quad (5)$$

where  $\rho' C'$  are the quantities for the impacted solid.

When a liquid cylinder of radius  $r$  impacts the 'water-hammer' pressures last until release waves pass to the central axis, i.e. for a time  $t$  given by

$$t = r/C \quad (6)$$

For a cylindrical jet of head diameter 3 mm,  $t$  is therefore  $\sim 1 \mu s$ . Once steady flow has been set up pressures given by incompressible flow should result with a stagnation pressure of

$$P = \frac{1}{2} \rho V^2 \quad (7)$$

Since  $V \ll C$  these pressures are significantly less than those given by equation 3. This is emphasized if we look at the ratio of compressible to incompressible pressures obtained using equations 3,4 and 7,

$$P_C/P_I = 4 + 2 C_0/V \quad (8)$$

Thus for impact velocities of 300 and 600  $\text{ms}^{-1}$  we have, for example, values of  $P_C/P_I$  equal to 14 and 9 respectively. This explains why it is the pressures generated in the first instants of impact that dominate the behaviour in the velocity range up to  $\sim 1000 \text{ms}^{-1}$ .

As Bowden and Field (1964) showed, spherical drops will also generate 'water-hammer' pressures. When the drop first impacts the radius of contact increases initially at a velocity greater than  $C$ ; thus flow is not possible and the impacted liquid must be compressed and give  $\rho C V$  pressures. They showed that the radius of this region,  $x$ , was given by

$$x = \frac{RV}{C} = \frac{RV}{C_0(1 + 2V/C_0)} \quad (9)$$

where  $R$  is the drop radius.

The time for this stage to be reached can be shown to be  $\sim \frac{RV}{2C^2}$ . Adding to this the time for release waves to reach the centre (i.e.  $\frac{RV}{C^2}$ ) gives a duration,  $t$ , for the  $\rho C V$  pressures of

$$t \sim \frac{3}{2} \frac{RV}{C^2} \quad (10)$$

One of the most important points about drop impact is that the region of high pressure (equation 9) and the duration (equation 10) depend on the drop radius in the contact area. This has various consequences. First it explains why the large drops in a rain field are the most damaging. Secondly it tells us that if a drop is oscillating it will be much more damaging if it impacts when its colliding surface has a large  $R$  value. Thus a drop of, for example, 5 mm mean diameter could, under certain conditions, give similar damage to a much larger drop. Thus the important radius in discussing drop damage is not the

mean size of the largest drops which impact but the maximum radius they achieve when oscillating.

(ii) High edge pressures

There is now evidence that this high pressure area described by equation 9 is surrounded by an annular region of even higher pressure; possibly associated with the onset of jetting. Heymann (1959) has predicted values of  $3 \rho C V$  for this region. Johnson and Vickers (1973) in experiments with large (50 mm diameter), low velocity ( $\sim 50 \text{ ms}^{-1}$ ) jets found higher edge pressures compared with central pressures in the ratio 2.25. Rochester and Brunton (1973, 1974) reported a ratio of 2.6 when 5 mm diameter discs of water were impacted edge on at  $100 \text{ ms}^{-1}$ .

We have also obtained evidence for high edge pressures from our high-speed camera records. In figure 15a we see four frames from an Imacon sequence taken at  $1 \mu\text{s}$  per frame. In frame 1 the jet has just struck the PMMA target and a shock front, f, passes into the material. Behind this is a front, labelled e, which is made up of two lobes, one on each side of the impacting jet. These lobes we believe are due to high pressure regions developed at the jet edge when fast outward flow begins. By frame 2, pulses from these edge sources have intersected and reinforced giving the dark region behind the main front. Further back the sub-surface damage, labelled d, can be seen developing. In frame 4 a second weaker front marks the rear of the main high pressure region (figure 5 showed the later development of these two parallel fronts which mark the limits of the 'water-hammer' pressures). The pressure lobes, e, clearly appear at the right position and time to be consistent with the edge pressure idea. The photograph given in figure 15(b) shows that the high edge pressures can also be detected in the liquid. In this example

a PMMA surface impacts a stationary two-dimensional water drop (for a discussion of the technique for producing 2-D drops see Brunton and Camus 1970, Camus 1971). This is a single shot Schlieren photograph. The high pressure regions at the drop edge, where jetting is starting, can be clearly seen, as also the shock front passing through the liquid.

(iii) Region c

The region c taken from damage studies (see insert on figure 9) is invariably larger than the region of diameter  $2x$  given by equation 9. As indicated in the preceding section this is very likely due to the extra annular region of high pressure. Another effect which has to be considered is the finite compressibility of the material (equation 9 assumes a rigid target). This, however, turns out to be a small correction of only a few percent. The reason for this is that although the finite compressibility allows the material to deform more easily, it also means that lower pressures are generated for a given impact velocity (see equation 5). In other words two effects tend to cancel.

If we rewrite equation 9 putting  $c = 2x$  and introducing a function  $\alpha(V)$  to take care of the edge pressure effect, we obtain, for velocities in  $\text{ms}^{-1}$

$$\frac{c}{d'} = \frac{V \alpha(V)}{C_0(1 + 2V/C_0)} = \frac{6.67 \times 10^{-4} V \alpha(V)}{(1 + 2V/C_0)} \quad (11)$$

Experimentally it was shown earlier (see equation 1) that  $c/d' \sim 6.16 \times 10^{-4} V$ , also that for a velocity of impact of  $304 \text{ ms}^{-1}$  that  $c/d'$  was  $\sim 0.2$ . It is interesting to note that our two correction terms in equation 11 must almost cancel (i.e. because  $6.16 \times 10^{-4}$  is close to  $6.67 \times 10^{-4}$ ). Analysis of the results shows that the function  $\alpha(V)$  is

represented closely by  $1 + 3.3 \times 10^{-4} V^{1.2}$ , thus

$$\frac{c}{d'} = \frac{V(1 + 3.3 \times 10^{-4} V^{1.2})}{C_0 (1 + 2V/C_0)} \sim 6.16 \times 10^{-4} V \quad (12)$$

Whatever the details of these formulae the important point is that crater dimensions with drop impact depend on (i) drop size (ii) impact velocity.

(iv) Pressure transducer measurements

One of the objections which has repeatedly been advanced to the use of pulsed jets in modelling raindrop impact is that the pressure pulse from a jet will have a different distribution and will be larger than for a typical raindrop. High speed photography of jets seems to confirm these fears since they show an apparently coherent jet, meant to model a large raindrop, colliding with the surface for typically 100  $\mu$ s.

Arguments have already been given above which show that the initial  $\rho C V$  pressures are very much higher than the steady-state incompressible flow pressures in the velocity regime of interest. The object of the experiments described in this section was to make pressure recordings so as to settle this point equivocally. This part of the work was performed by Dr J-J Camus.

A transducer was required with very large band width and high strength to withstand pressures up to about  $1000 \text{ MN/m}^2$ . The adopted design was that of the simple bar gauge scaled down to provide high spatial resolution and increased band width at the same time.

Baganoff (1963) constructed capacitive pressure gauges with rise times of 0.1  $\mu$ s and suggested that bar gauges using piezoelectric ceramics would be an attractive alternative but that they were ruled out by problems of capacitive loading on the piezoelectric element. This is not

a serious limitation with lead zirconate titanate piezoelectric ceramics where one only wants to record very brief events; that is events, as in this case, of duration less than time constant of the input to the oscilloscope ( $\approx 100 \mu\text{s}$ ) but where the charge developed is sufficient to give a reasonable deflection of the beam.

It was decided that the minimum practical diameter for the transducer would be about 0.3 mm. The minimum convenient thickness was about 0.1 mm. Taking the compression wave velocity in the PZT4 ceramic used as about  $4 \times 10^6 \text{ mm s}^{-1}$ , the estimated rise time would be approximately 30 ns; in fact, the thickness used varied between 0.1 and 0.2 mm. The PZT4 disc is mounted on a steel backing rod which provides the best acoustic match at the interface (about  $40 \times 10^6 \text{ Kg/s}^{-1} \text{ m}^{-2}$ ). Propagation of a pulse down the length of the backing rod will begin to be attenuated for those Fourier components whose wavelengths are less than or equal to the rod diameter. Another limit on the bandwidth is therefore  $4 \times 10^6 / 0.3 \approx 10 \text{ MHz}$  for non-dispersive pulse propagation (Skalak 1957, Miklowitz 1958). This, in conjunction with the small physical size of the gauge, was considered adequate.

The gauge was made by cutting a cylinder of material out of a commercially available block of PZT4 with an ultrasonic drill using a hypodermic needle of internal diameter about 0.3 mm. The direction of the electric polarization was arranged to be along the axis of the cylinder. This was then mounted with glue on a flat substrate for ease of handling and cut like a salami with a flat cutter on the ultra-sonic drill or sliced by hand with a razor blade under a low-power stereoscopic microscope. At first, each disc in turn was placed in a small holder and one of its faces was smoothed on very fine emery paper (grade 600); but it was found that the resultant surface was not smooth enough to bond adequately to the backing rod (see Sittig 1972). Subsequently therefore, the surface to be

bonded was further polished down to 3  $\mu\text{m}$  diamond paste. The surviving discs were flow bonded to the similarly polished ends of 0.3 mm diameter steel wires to act as backing rods, this again being done by hand under a low power microscope. The adhesive used was standard epoxy resin.

Next, a hole of diameter slightly in excess of that of the backing rod was drilled through a small phenolic resin/cloth block to accommodate each rod. Rod and ceramic discs were then pushed into the holders, the ends of the backing rods tapering off into epoxy adhesive (see f, figure 16). The free face of the ceramic disc, a, was made flush with the holder surface and polished flat on 600 abrasive paper. Finally a silver paint electrode, b, was applied to the front face of the transducer, the backing rod acting as electrode, e, to the back face. The electrodes were connected directly via 70  $\Omega$  cable to the input of an oscilloscope. Figure 17(a) shows a typical response trace in which the peak signal has been allowed to go off the screen to display the fine structure of the decay as the high pressure is released. The impact was that of a 1.5 mm water jet at about 300  $\text{ms}^{-1}$  at a distance of 10 mm from the nozzle. There is a remarkable freedom from ringing in the transducers. It is also apparent that the peak half width is under 1  $\mu\text{s}$ .

Calibration of the transducer was only carried out in a few cases since the exact maximum pressure level was not of overriding importance in this work and the calibration procedure is very elaborate. We used a method similar to that of Crook (1952) as adapted by Rochester and Brunton (1973). The gauge was held securely in a massive clamp and a large steel ball was placed in contact with the transducer's sensitive area. A second steel ball of equal size was swung against this arrangement from a measured height. The output was displayed on the oscilloscope.

It can then be shown that

$$m \sqrt{2g(h_1 + h_2)} = \frac{c}{kd} \frac{3}{2} V_{\max} \tau$$

where  $m$  is the mass of the ball,  $h_1$  the height from which it falls,  $h_2$  the height of rebound,  $g$  the acceleration of gravity,  $V_{\max}$  the maximum gauge output,  $\tau$  the duration of the impact,  $d$  the piezoelectric constant of the ceramic,  $k$  the gauge constant and  $c$  the combined capacitances of ceramic, pickup, leads and oscilloscope input.

$m$  and  $c$  were measured and  $h_2$ ,  $V_{\max}$  and  $\tau$  noted for a range of  $h_1$ . A graph of  $m \sqrt{2g(h_1 + h_2)}$  versus  $\frac{c}{kd} \cdot \frac{2}{3} V_{\max} \tau$  was plotted and was found to be linear within 7%.

The product  $kd$  of the piezoelectric and gauge constants was found to be, typically,  $0.12 \times 10^{-8}$  m/V. Now the pressure on the gauge during impact is given by

$$p = \frac{c}{kdA} \cdot V$$

where  $V$  is the output voltage and  $A$  is the area of the gauge. Thus, in figure 17(a),  $p \approx 1.20 \times V$  MN/m<sup>2</sup>.

Most of the tests were carried out with a jet velocity of about  $300 \text{ ms}^{-1}$ . The nozzle size was generally 2.8 mm in diameter to model a very large drop and provide a large impact site. Typical oscilloscope traces are drawn in figure 17. Figure 17(b) is typical of pressure traces in the centre of the impact region, which was about 6 mm in diameter. Maximum pressure in that case was  $360 \text{ MN/m}^2$ , that is approximately 0.8 times the  $\rho C_0 V$  pressure and 0.57 times the  $\rho C V$  pressure.

It is immediately obvious that the pressure pulse from a jet must produce extraordinarily high rates of strain. Thus while the best direct measurement of rise time was, previously,  $1 \mu\text{s}$ , figure 17(b) shows that a

peak pressure is reached within  $0.1 \mu\text{s}$  which results in an upwards revision of strain rates of an order of magnitude. Moreover total duration of the peak is only about  $1 \mu\text{s}$  with a decay time again of about  $0.1 \mu\text{s}$ .

Figures c and d show other traces. Again there is a rapid rise in a fraction of a microsecond to a high pressure which lasts for  $\sim 1 \mu\text{s}$ . The peak pulses reached values of between  $0.7$  and  $0.8 \times \rho C_0 V$ . Very important from the point of view of rain drop modelling are the low pressures which then result.

The question of why the pressures fall short of the full water-hammer pressure is interesting. In our view it is not because the head of the jet has a density less than unity since similar values have been recorded for impacts with drops. In their work, Johnson and Vickers (1973) recorded a central pressure of  $0.66 \rho C V$  while Rochester and Brunton (1973, 1974) obtained  $0.7 \rho C_0 V$  ( $\sim 0.6 \rho C V$ ). Since there appears to be no reason why the water-hammer pressure should not result it leaves various possibilities (i) that there is an unidentified error (for example rate effect or non-linearity) that is affecting all measurements with piezoelectric transducers in this high-strain rate situation, (ii) trapped gases between the drop and the target give a 'cushioning' effect (this though is unlikely to be large), (iii) that the impact produces electrical and <sup>magnetic</sup> effects which modify the recorded signals. It is hoped that future work will clarify this question.

One of the reasons for designing such small pressure transducers was to be able to record pressures at various points in the impact area. Unfortunately, because of the very high pressures developed by impacts at about  $300 \text{ ms}^{-1}$  it was found that the transducers, no matter how carefully constructed, could not withstand more than about 6 impacts before becoming unreliable. This precluded scanning across the impact region since several traces at each point are essential and this implies a much greater

resistance to the impact stress than could be achieved with these transducers. However, for lower velocities of impact the instrumentation, as developed here, would be capable of investigating spatial pressure distributions.

#### 7. Residual Strength of Glass after Liquid Jet Impact

Because of the dependence of strength properties on the severity of, possibly, invisible defects in a glass surface, assessment of impact damage is more realistically carried out by considering the residual strength of the material, and not by damage size or microscopic appearance. A variety of test methods are available for measuring the strength of brittle solids. These include stressing the specimen in pure tension, bend tests, indentation loading, ring-on-ring methods, and techniques involving hydrostatic loading (Bowles 1974).

In this work the residual strength of glass samples following a single liquid impact has been determined using a uniform hydrostatic loading system to produce a biaxial stress distribution on the surface of the specimens. Samples are discs of diameter 57 mm and nominal thicknesses 3 mm and 6 mm. These are centrally impacted by water jets of velocities in the range  $200 - 600 \text{ ms}^{-1}$ , and then tested to failure in the pressure tester, the damaged surface being in tension. In our work on residual strength of glass after impact many of the above testing techniques were unsatisfactory in that failure frequently started at the specimen edge. However, with a hydraulic 'blow-out' method it was possible to overcome this difficulty. The technique also proves to have several other advantages.

A schematic diagram of the pressure tester is shown in figure 18. The

specimen, in the form of a 51 mm disc of any thickness up to 10 mm, is held against a steel support ring. A neoprene diaphragm transmits the uniform hydrostatic pressure across the entire surface of the disc. The apparatus is constructed of mild steel, and is designed to operate with hydraulic fluid up to 12 MPa. The neoprene diaphragm and steel support ring are both easily replaceable.

Simple plate theory gives the following results for the radial and tangential components of the stress at radius  $r$ :

$$\sigma_r = \frac{3Pa^2}{8t^2} \left\{ (3 + \nu) \left(1 - \frac{r^2}{a^2}\right) \right\}$$

$$\sigma_t = \frac{3Pa^2}{8t^2} \left\{ (3 + \nu) - (1 + 3\nu) \frac{r^2}{a^2} \right\}$$

(Timoshenko 1941, Roark 1965)

where  $\sigma_{r,t}$  is the radial or tangential component of surface stress

$P$  is the applied pressure

$a$  is the disc radius

$\nu$  is Poissons ratio for the specimen material

$t$  is the disc thickness.

The radial variations of the stress components are illustrated in figure 19.

The formulae apply to the case of a circular disc freely supported at its edges, with no overhang outside the support. At a given radius,  $r$ , the stress components become:

$$\sigma = K_r P/t^2, \text{ where } K_r \text{ is a constant.}$$

Calibration of the test can be carried out using conventional resistance strain gauge techniques. Some results for a 6mm thick soda-lime silicate glass disc are presented in figure 20. Since the thickness of glass specimens of a given nominal size are likely to vary, the results are plotted as  $\sigma \times t^2$ ; the curves therefore apply to a range of thickness of glass. The measurements plotted are the central stress, and the radial and tangential components at a radius of 10mm. For the central stress,  $\sigma_c = \frac{K_c P}{t^2}$ , the theory given above predicts the value of  $K_c$  to be  $673 \text{ mm}^2$ . This compares well to the measured value of  $670 \pm 20 \text{ mm}^2$ . However, a correction for the overhang of the disc outside the support ring was derived by Mansfield (1963), and in this case it leads to a 3% reduction in the theoretical value of  $K_c$ .

An important consideration in this type of test is the support conditions of the disc. A glass disc pressed against the steel retaining ring will usually fail from the edge. This is due to the high local stress concentrations of the irregular contact, and also to roughly cut and unpolished discs having the most serious flaws at the perimeter. However, it was found that a suitable gasket of paper or polymer sheet inhibited such undesirable edge effects. The most convenient gasket material to use was a proprietary self-adhesive polymeric sheet, either in the form of disc or a narrow annulus. With such a gasket, failure rarely occurred at the disc edge.

The simple theory assumes a completely free knife-edge support, a condition which is obviously not realised in the practical arrangement. However the calibration has demonstrated that the linearity of the stress-pressure relationship is not significantly affected by the non-ideal support, and the agreement between the measured and predicted values for the central stress are also very close. It must be concluded that after calibration the edge restraints of lateral friction and the effect of

overhang can be ignored.

When unimpacted discs were tested, the failure points were widely distributed over the tension surface, but mainly fell within a 10 mm radius. This is in accordance with the known strength properties of brittle glasses, where surface flaws are the initiating points of fracture. The stress distribution is such that the stress components vary in magnitude comparatively slowly over quite a large radius (the radial component is one half of its maximum central value at a radius of  $\approx 17$  mm). Thus the most serious flaw, wherever it occurs, is likely to initiate failure. When failure nucleated near the centre of the disc, the fracture pattern consisted of a large number of radial fractures. Figure 21 shows such a disc that has been tested and the initiating point, P, is about 7 mm from the centre. The fractures all extend from this point, and most of them bifurcate. Plates which failed at a lower stress have a correspondingly smaller number of these radial fractures.

The hydraulic pressure tester is easy to construct and its behaviour agrees well with simple theory. The main advantages of its use can be summarized:

- (i) Edge failures which cause difficulty with tensile testing or three- or four-point bending are largely eliminated.
- (ii) Compared with the standard ring-on-ring test, the advantages are:
  - (a) The test region extends almost to the edge of the specimen, in contrast to the ring-on-ring test where only a small area within the inner ring is suitable.
  - (b) There is little stress concentration from mechanical pressure.
  - (c) There is much less effect due to warped plates.
- (iii) Small specimens can be used, and the method can easily be further miniaturized.
- (iv) The method is extremely rapid in operation, and facilitates the

production of the large number of results necessary for statistically meaningful strength measurements in glass.

- (v) An additional advantage in the present work is the circularly symmetrical stress field. The impact damage consists largely of radial or circumferential fractures, and the biaxial tensile stress field in the outer surface of the glass ensures that any crack orientation is subjected to a similar value of the perpendicular tensile stress component.

Some results are now presented which examine the residual strength of samples of two types of glass impacted with water jets in a range of velocities. A large number of 51 mm diameter discs were centrally impacted by jets from two nozzle sizes, 0.8 mm and 1.6 mm. The specimens were then broken in the pressure tester with their impacted faces on the tension side. The strain rate was  $\sim 10^{-4} \text{ sec}^{-1}$ . The failure pressures and positions were recorded, and a value of the fracture stress at the initiating point estimated. Figure 22 shows the results obtained from 6 mm thick discs of soda-lime silicate glass; each point is the average of at least six samples. It is found that a single impact has negligible effect on the strength properties of the discs until a certain jet velocity is reached. Then the mean fracture stress falls off, initially very rapidly, with increasing jet velocity. The critical velocity is approximately  $300 \text{ ms}^{-1}$  for the 0.8 mm nozzle and  $200 \text{ ms}^{-1}$  for the 1.6 mm nozzle. It is significant to note that this rapid decrease in strength occurs before visible damage is apparent in the samples! Damage becomes easily visible at jet velocities in the region of  $420 \text{ ms}^{-1}$  and  $270 \text{ ms}^{-1}$  for the 0.8 and 1.6 mm nozzles respectively.

It is important to realise the inherently statistical nature of these results. When strength reduction first occurs it does so only in

some of the specimens. As the impact velocity is increased there is a greater probability that a given specimen will be reduced in strength, so that at high velocities,  $500 \text{ ms}^{-1}$  say, all specimens show some strength reduction. In the intermediate region, the specimens fall into two groups: those which fail at low stresses and have been damaged by the liquid impact, and those which fail at stresses comparable to the original strength of the glass. As the velocity of impact is increased the number of specimens in the former group increases.

Results can be presented in several ways to demonstrate this.

- (i) Averaging out all fracture stresses at a given impact velocity irrespective of which group they fall into. This gives a good indication of the probability of an impact producing strength reduction in the material (figure 22).
- (ii) Plotting the two groups separately with overlap in the velocity region where fracture stresses can fall into either group (figure 23). This gives a truer indication of actual failure stresses likely to be realised in practice but gives no indication of the relative probabilities of their occurring.
- (iii) A plot of fracture stresses obtained from individual experiments (figure 24). Two types of failure are recorded; those from non-central fracture origins corresponding to no reduction in strength, and failure from a central origin, indicating a reduced strength due to liquid impact damage.

In addition to the commercially available soda lime silicate glass, a number of specimens of a calcium aluminate type glass have been tested using the liquid impact plus residual strength measurement technique. Results are presented in figure 25 for this glass, the only calcium aluminate available in sufficient quantities to enable a reasonable residual strength curve to be plotted. Impacts were from the 0.8 mm

nozzle. Its initial fracture strength in the pressure tester was determined to be  $126 \pm 25$  MPa, compared with  $75 \pm 4$  MPa for the Pilkington soda lime glass. Under liquid impact for 0.8 mm jet it showed a better performance than the soda lime glass; samples beginning to fail due to reduced strength above  $\sim 350 \text{ ms}^{-1}$ , compared with  $\sim 300 \text{ ms}^{-1}$  for the soda lime. Even after strength reduction occurred the calcium aluminate proved to have a higher residual strength than the soda lime until  $450 - 500 \text{ ms}^{-1}$  impact velocity, after which the residual strengths of both glasses were  $\sim 30$  MPa. This reflects the higher initial strength of the calcium aluminate to a certain extent, since samples which did not show reduced strength are included in the calculation of the mean fracture stress at each velocity. At velocities in excess of  $400 \text{ ms}^{-1}$  if damage did occur, then reduced strengths were similar, whatever the type of glass.

The shape of the residual strength curves is interesting. Their characteristic features are the low velocity plateau, the rapid drop of strength over a narrow velocity region and then the slowly decreasing high velocity region. The pressures and durations caused by jet impact will be given by equation 5 and 6. The wave causing fracture initiation around the loaded area is the Rayleigh surface wave. A fracture will initiate when a critical stress intensity is reached at the tip of a microdefect. The fact that there will be a distribution of defects accounts for the statistical spread of the results. However, until the velocity (and hence the stress) exceeds a certain value the microcracks will not extend in length; this explains the initial plateau. (Note that since the pressure pulse duration is  $\sim 1 \mu\text{s}$  all sub-critical crack growth

effects can be neglected). Once a crack initiates it will extend rapidly (accelerating up to a maximum velocity, which for soda-glass is about  $1500 \text{ ms}^{-1}$ ). This explains the rapid fall off in strength. However the crack will only extend while the pulse is on and so will remain short and discrete rather than extending to the boundary of the specimen. For example if it travels at say  $750 \text{ ms}^{-1}$  for  $1 \mu\text{s}$  it will extend from micron dimensions to  $\sim 0.75 \text{ mm}$  length. This macroscopic crack explains the final part of the residual strength curve. Similar shaped curves have been reported by Evans (1973) on strength degradation of ceramics due to Hertzian fractures initiated by solid spherical particle impact.

#### 8. Conclusions

(a) This report shows that it is possible to obtain a reasonably accurate simulation of drop impact using water jets. No claim is made that the simulation is perfect since there is always the possibility of small differences in pressure distribution or duration. However, by suitable scaling, jets and drops can be related so that at a particular velocity 'water-hammer' pressures are produced over similar sized areas and for similar durations.

(b) Advantages of the jet method are ease of operation, the ability to simulate large drop sizes and the fact that the target specimen is stationary. Having a stationary target is important with brittle specimens, with specimens of complex shape and when residual strength measurements are required.

(c) Details are given for producing a gun apparatus for firing jets. If chambers are designed and loaded to the specifications in this report reproducible stable jets will be obtained. These jets can simulate drops from  $\sim 1 \text{ mm}$  to  $\sim 50 \text{ mm}$  in the velocity range up to  $\sim 1000 \text{ ms}^{-1}$ . It is possible to produce jets of even higher velocity by using higher projectile

velocities or by making the chamber design more efficient (the ratio of jet velocity to projectile velocity can be made  $\sim 10\times$  by careful design. See for example, Rhyming 1973).

(d) A gas gun is described capable of firing specimens at suspended drops with velocities up to  $\sim 400 \text{ ms}^{-1}$ . It was relatively simple to construct. It has proved versatile and useful.

(e) An image converter camera, the Imacon, was used extensively for jet and impact studies. Its advantages were that it was synchronisable from the event, could be used with conventional light sources and gave records on 'Polaroid' film. However, although such a camera was essential for this project, less sophisticated methods could be used for future erosion studies using the jet method. Suggestions are made in section 5 as to how projectile and jet velocities could be recorded using photocells and spark photography.

(f) Section 6 of this report discusses at length the question of relating jet and drop sizes. It gives data on the damage patterns produced by drops as functions of drop diameter and velocity. Similarly it gives information on the damage produced by different sized jets, again for a range of velocities. These results are analysed and combined to produce curves of equivalent drop size for the jets used (see figure 13).

(g) When a drop impacts, the size of the damage region depends on both drop size and velocity. See, for example, equation 9 and figures 9 and 10. This is of great importance in explaining why the large drops in a rain field are the most damaging (the water-hammer pressures cover a larger area and last longer). If a drop is oscillating the important dimension is the radius of curvature at the impact surface. This means that a drop can act effectively as a much larger drop. This needs to be remembered when assessing the hazard of collisions with large rain drops: it is not the mean size of the largest raindrop that is important, but

the largest radius of curvature that this drop can reach when oscillating.

(h) Water drops of diameter greater than  $\sim 2$  mm are difficult to suspend. This problem was overcome by using gelatine/water drops for the size range 2-6 mm (see figure 10).

(i) If the jet method had produced perfectly cylindrical jets of diameter equal to the orifice dimension then the specimen area subjected to water-hammer pressures would have remained constant for all velocities. In practice the jets produce a 'mushroom' head (see section 6b) and its dimension is a function of velocity and orifice size. However, at a stand-off distance of 10 mm the jets behave reproducibly. Curves are given for the size of damage patterns produced by the jets (figures 11, 12). The fact that the jets produce a 'mushroom' head with a slightly curved front face is almost certainly beneficial in allowing the jets to simulate the drop impacts accurately.

(j) In section 6(d) the pressure pulses produced by liquid drop impact are discussed. The point is made that for the range of velocities of interest here, the water-hammer pressures greatly exceed the stagnation pressures produced by incompressible flow. Thus it is always the first instant of impact which is of prime importance with both jet and drop impact. Pressure traces taken with very small pressure transducers confirm these conclusions.

(k) The pressure transducer system developed for these experiments is capable of great spatial resolution. The usefulness of this feature was limited at the high velocities we were interested in ( $\sim 300 \text{ ms}^{-1}$ ) since sufficient strength for multiple impacts ( $> 10\times$ ) could not be achieved. However, for velocities of impact of  $\leq 100 \text{ ms}^{-1}$  this problem would not exist.

(l) There now seems ample evidence that high edge pressures exist in an annular region around the main 'water-hammer' area. They have been observed for both jet and drop impact. Values of between 2 and  $3 \times \rho C V$

seem possible. Present evidence points to their being associated with the onset of fast radial jetting.

(m) The importance of quantitatively assessing damage is emphasized in this report. Section 7 describes a hydraulic test apparatus for measuring 'residual strengths' and discusses residual strength data. An important result from this work is that large strength losses can take place before the damage reaches visible dimensions; this clearly has practical importance. Some progress has been made in predicting the shape of the residual strength curves.

#### Acknowledgements

This research was sponsored by the Procurement Executive, Ministry of Defence. The Imacon camera was purchased with an SRC grant to the Cavendish Laboratory.

We would like to thank Dr N.S. Corney and A.A. Fyall for many useful discussions during the course of this work. The advice of B.G.I.R.A. (Sheffield) when we were assessing methods of testing glass sample strength is gratefully acknowledged.

References

1. Baganoff D. 1964, Rev. Sci. Inst. 35, 288.
2. Birkhoff G., MacDougall D.P., Pugh E.M. and Taylor G.I. 1948,  
J. Appl. Phys. 19, 563.
3. Bowden F.P. and Brunton J.H. 1958, Nature 181, 873.
4. Bowden F.P. and Brunton J.H. 1961, Proc. Roy. Soc. A 263, 433.
5. Bowden F.P. and Field J.E. 1964, Proc. Roy. Soc. A 282, 331.
6. Bowles R. 1974 (Chairman) "Strength Testing of Glass and Glass Pro-  
ducts" (Charleroi, Belgium: Inst. Nat. du Verre).
7. Brunton J.H. 1961, Proc. 5th Int. Cong. on High-speed Photography,  
p.503.
8. Brunton J.H. and Camus J-J. 1970, Proc. 3rd Int. Conf. on Rain  
Erosion and Allied Phenomena, Farnborough, p.327.
9. Camus J-J. PhD Thesis, Cambridge 1971.
10. Crook A.W. 1952, Proc. Roy. Soc. A 212, 377.
11. Evans A.G. 1973, J. Am. Ceram. Soc. 56, 405.
12. Field J.E., Camus J-J, Gorham D.A. and Rickerby D.G. 1974, Proc. 4th  
Int. Conf. on Rain Erosion, Meersburg.
13. Frilingel F.B.A. 1965, "High-speed Pulse Technology" Vol.II, Academic  
Press.
14. Gorham D.A. 1974, PhD Thesis, Cambridge.
15. Harper E.Y., Grube G.W. and Chang I-D. 1972, J. Fluid Mech. 52, 565.
16. Heyman F.J. 1969, J. Appl. Phys. 40 (13) 5113.
17. Hutchings I.M. and Winter R.E. 1975, J. Phys. E. 8, 84.
18. Johnson W. and Vickers G.W. 1973, J. Mech. Enging Science 15, 302.
19. Luy H. and Schade R. 1956, Proc. 2nd Int. Cong. on High-speed  
Photography, p.59, Dunod. Paris.
20. Mansfield E.H. 1963, J.R. Aero. Soc. 67, 671.
21. Miklowitz J. 1958, Proc. 3rd U.S. Nat. Cong. Appl. Mech. 215.

22. Roark R.J. 1965, 'Formulae for Stress and Strain', 4th edition, McGraw-Hill, p.216.
23. Rochester M.C. and Brunton J.H. 1973, Proc. 76th Annual Meeting Amer. Soc. for Testing Materials, Philadelphia.
24. Rochester M.C. and Brunton J.H. 1974, Proc. 4th Int. Conf. on Rain Erosion and Associated Phenomena, Meersburg.
25. Rhyning I.L. 1973, J. Appl. Math. and Physics (ZAMP) 24 (10) 150.
26. Simpkins P.G., Bales E.L. 1972, J. Fluid Mech. 55, 629.
27. Sittig E.K. 1972, Physical Acoustics, eds. Mason W.P. and Thurston R.N., Academic Press, London.
28. Skalak R. 1957, J. Appl. Mech. 24, 59.
29. Taylor G.I. 1950, Proc. Roy. Soc. A 201, 192.
30. Timoshenko S.P. 1941, 'Strength of Materials' Part II, 2nd edition (London: MacMillan) p.140.

Figure Captions

- Figure 1 (a) Dimensions of the steel extrusion chamber, filled with water to positions 'E' or 'F'.  
 (b) Momentum exchanger piston for low jet velocities.
- Figure 2 Calibration curve for the 0.8mm diameter extrusion nozzle. Helium can be used in the gas gun to produce the highest jet velocities. The momentum exchanging steel plunger enables low velocities to be reached.
- Figure 3 Variation of jet velocity with orifice diameter at a constant slug velocity of  $175\text{ms}^{-1}$ . Logarithmic axes. Regions 1 and 2 correspond to approximate power law relationships of  $V_j \propto d^{-0.88}$  and  $V_j \propto d^{-0.44}$  respectively.
- Figure 4 Velocity conversion ratio for three exit orifice diameters.  $V_j$  - jet velocity;  $V_s$  - slug velocity; Nozzle sizes are 0.8mm, 1.6mm, and 2.4mm.
- Figure 5 Shadowgraph sequence of the impact of a  $750\text{ms}^{-1}$  water jet on to a PMMA block.  $1\mu\text{s}$  per frame. a, stress front induced by detached air shock; r, the reflected air shock; c, main compressive stress pulse of width w; h, head wave; s, shear front (poorly defined because of the nature of the optical system). d, sub-surface 'shear' failure; o, main ring crack.
- Figure 6 Frames selected from Imacon sequences of various jet sizes. All at  $10\mu\text{s}$  per frame. Slug velocity  $175\text{ms}^{-1}$  for each sequence. (a), (c) and (e) are jets produced with the exit portion of the chamber left empty (Position E). (b), (d) and (f) are with it full (position F). (a) 0.8mm nozzle, exit empty,  $980\text{ms}^{-1}$ ; (b) 0.8mm nozzle, exit full,  $910\text{ms}^{-1}$ ; (c) 1.6mm nozzle, exit empty,  $735\text{ms}^{-1}$ ; (d) 1.6mm nozzle exit full,  $700\text{ms}^{-1}$ ; (e) 2.4mm nozzle, exit empty, main jet  $550\text{ms}^{-1}$ , 'Munroe' jet  $800\text{ms}^{-1}$ ; (f) 2.4mm nozzle, exit full,  $525\text{ms}^{-1}$ .

Figure 7 'Munroe' jet, M, from a 1.6 mm diameter nozzle with the liquid/air interface concave inwards.  $10 \mu\text{s}$  per frame. Main jet velocity  $740 \text{ ms}^{-1}$ .

Figure 8 Single flash pictures of  $450 \text{ ms}^{-1}$  water jets from a 2.4 mm nozzle. Flash duration 150 ns. Distances of the jet from the chamber:  
(a) 10 mm, (b) 110 mm.

Figure 9 Liquid drop impact on PMMA. Crater dimensions (plotted non-dimensionally in terms of drop diameter,  $d'$ ) versus impact velocity. The various crater dimensions are given in the insert.

Figure 10 A plot of  $c$  versus drop diameter,  $d'$ , for an impact velocity of  $304 \text{ ms}^{-1}$ . Note that  $c$  increases approximately linearly with  $d'$  and that both the water and gelatine/water drops fall on the same line.

Figure 11 The variation of  $c$  with jet velocity for 0.4, 0.8, 1.6 and 2.4 mm nozzles. All results for a stand-off distance of 10 mm.

Figure 12 A replot of the data of figure 11 in non-dimensional form. The insert shows a cross-section through a typical jet showing the 'mushroom' head which is larger than the nozzle diameter.

Figure 13 Equivalent drop size produced by the four chambers versus velocity. The 0.4 mm chamber, for example, simulates 2 mm drop impact for a wide velocity range. Very large drops can readily be simulated.

Figure 14 'Talysurf' profilometer records of impacts by water jet and by spherical water drop on to PMMA. a)  $290 \text{ ms}^{-1}$ , 0.4 mm nozzle with momentum exchanger. Nozzle diameter marked. Vertical scale 100 x horizontal scale. b)  $260 \text{ ms}^{-1}$  PMMA projectile impacting 2 mm stationary water drop. Same scale as (a). (Specimen from A.A. Fyall).

Figure 15 (a) Imacon sequence of 2.8 mm nozzle jet,  $415 \text{ ms}^{-1}$ , impacting PMMA.  $1 \mu\text{s}$  per frame. f, is the main compressive part. e, is the subsidiary compressive wave originating from the edge of the contact zone. d is the sub-surface damage.

(b) Single frame image converter picture of moving PMMA plate impacting a stationary 5 mm two-dimensional water drop.

Schlieren optics enable high pressure regions inside the drop at the edge of contact area to be seen, and also the shock passing through the liquid. Impact velocity  $70 \text{ ms}^{-1}$ .

Figure 16 Schematic diagram of the pressure transducer mounting. a, 0.25 mm diameter, 0.1 mm thick transducer. c, backing rod. b,e electrodes to cathode ray oscilloscope (CRO). f, adhesive. d, holder.

Figure 17 Pressure transducer traces for jet impact at  $300 \text{ ms}^{-1}$ :

(a) 20 V/div.;  $2 \mu\text{s}/\text{div.}$

(b) 50 V/div.;  $2 \mu\text{s}/\text{div.}$ ; peak stress 360 MPA.

(c) peak stress 320 MPA.

(d) peak stress 290 MPa.

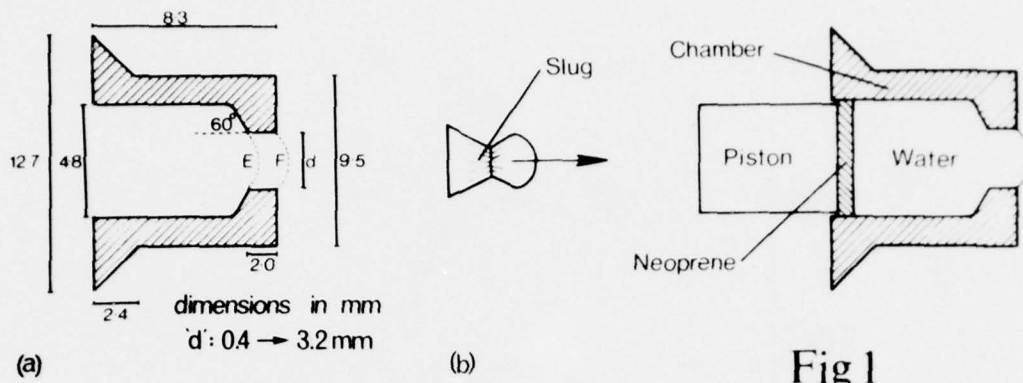
Note in all cases the rapid rise, the short duration ( $\sim 1 \mu\text{s}$ ) and the low steady flow pressure following the peak.

Figure 18 Section of pressure test apparatus for 51 mm glass discs. Overall diameter 133 mm, thickness 55 mm. Constructed from mild steel.

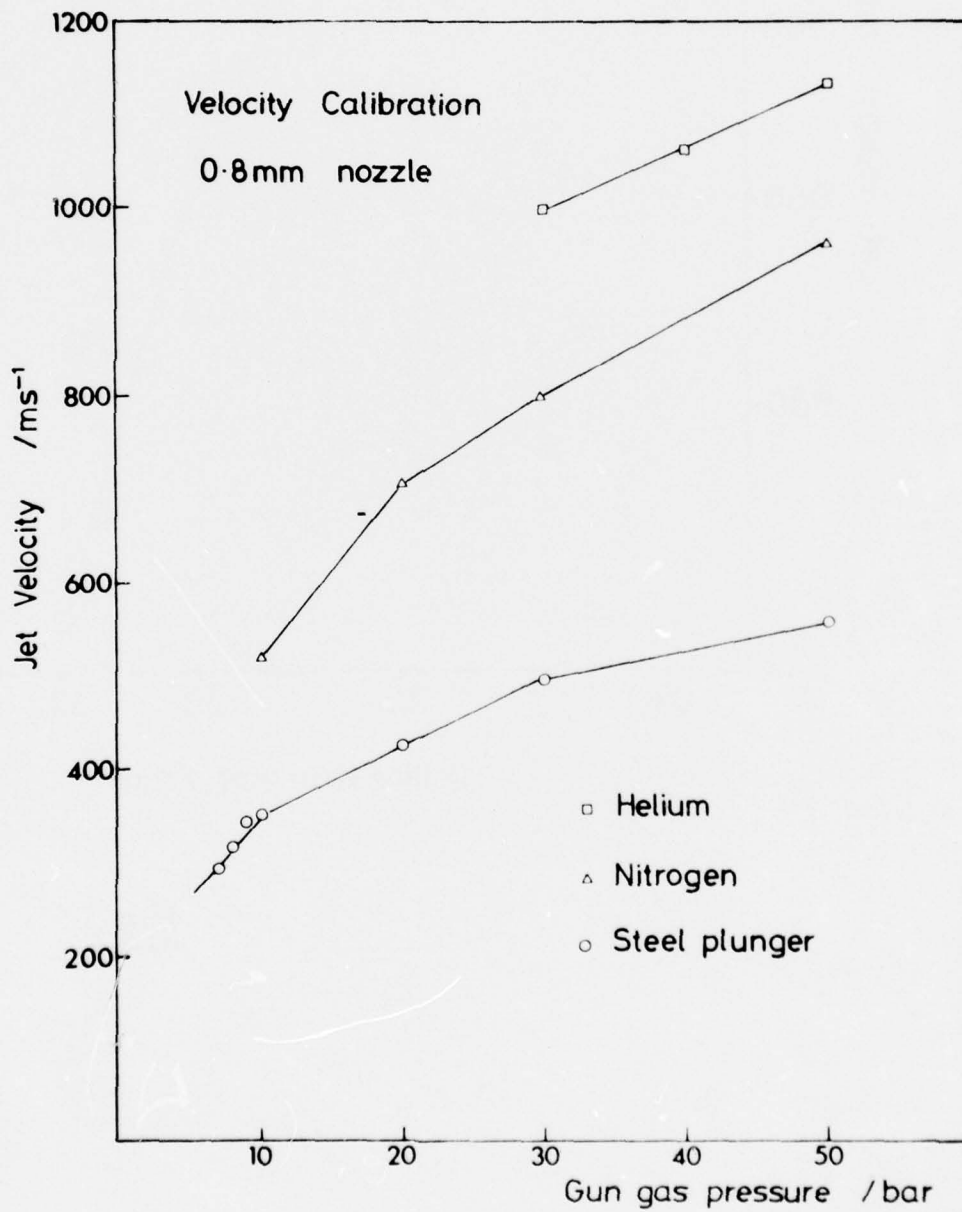
Figure 19 Theoretical and experimental variation of the radial and tangential stress components,  $\sigma_r$  and  $\sigma_t$ , across the disc surface.

Figure 20 Calibration of pressure tester: stress components determined from resistance strain gauge measurements are plotted against the applied hydraulic pressure. Circles:  $\sigma_c$ , central stress; squares:  $\sigma_t$ , tangential stress component at radius of 10 mm; triangles:  $\sigma_r$ , radial stress component at radius of 10 mm.

- Figure 21 Glass disc broken in the pressure tester. 51 mm diameter, 3 mm thick. Failure nucleated at point P.
- Figure 22 Average fracture stress, measured in the pressure tester, of 51 mm diameter 6 mm thick soda lime silicate glass discs after single water jet impact. Results are given for two nozzle diameters: squares: 0.8 mm; circles: 1.6 mm.
- Figure 23 Results presented in figure 5 for the 1.6 mm nozzle, replotted to illustrate the two distinct groups of specimens: those which are significantly weakened by a single impact, and those which are not.
- Figure 24 Individual fracture specimen results which are averaged in figures 5 and 6. The two distinct groups are clearly defined.
- Figure 25 Average fracture stress, measured in the pressure tester, of 51 mm diameter 3 mm thick calcium aluminate glass discs. Single jet impacts from the 0.8 mm nozzle.



**Fig 1**



**Fig 2**

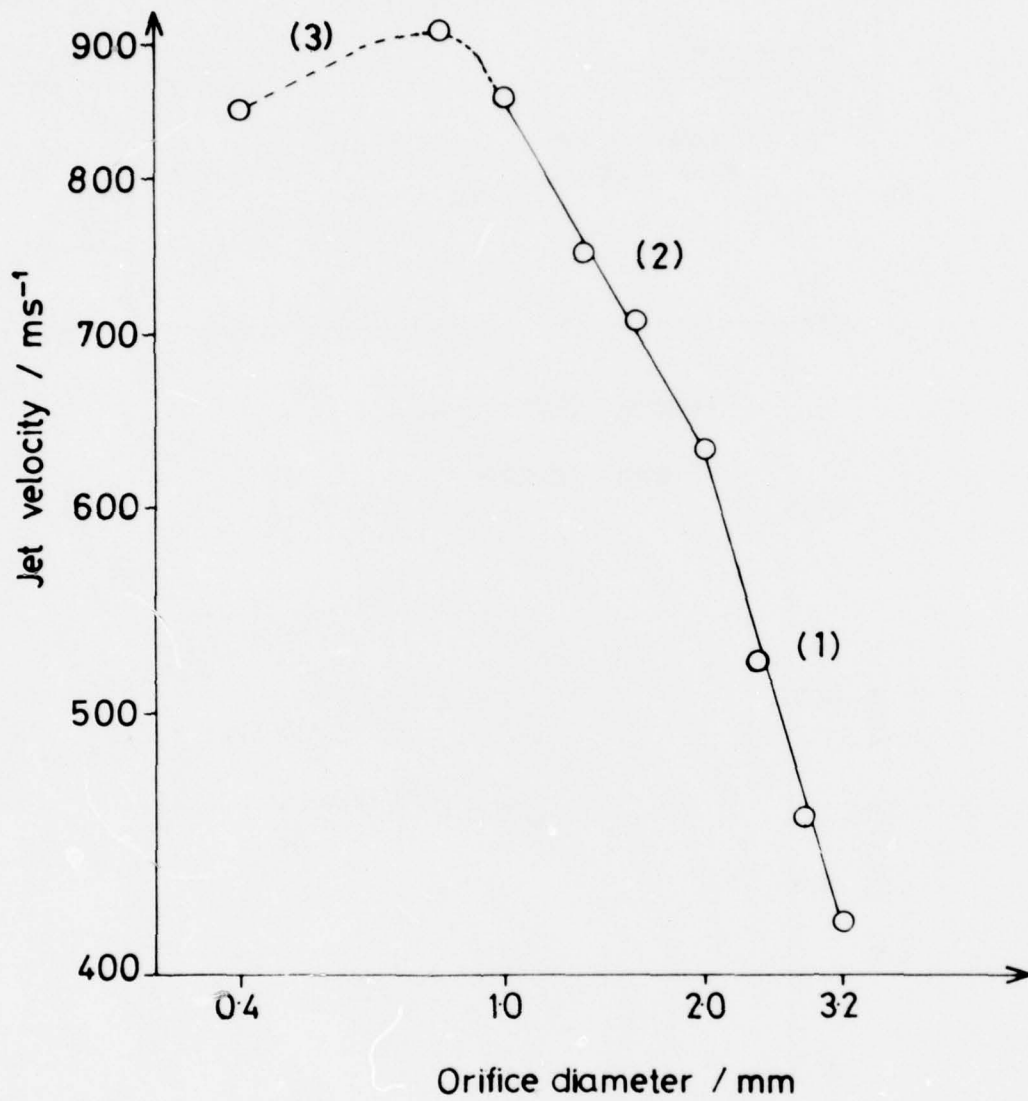


Fig 3

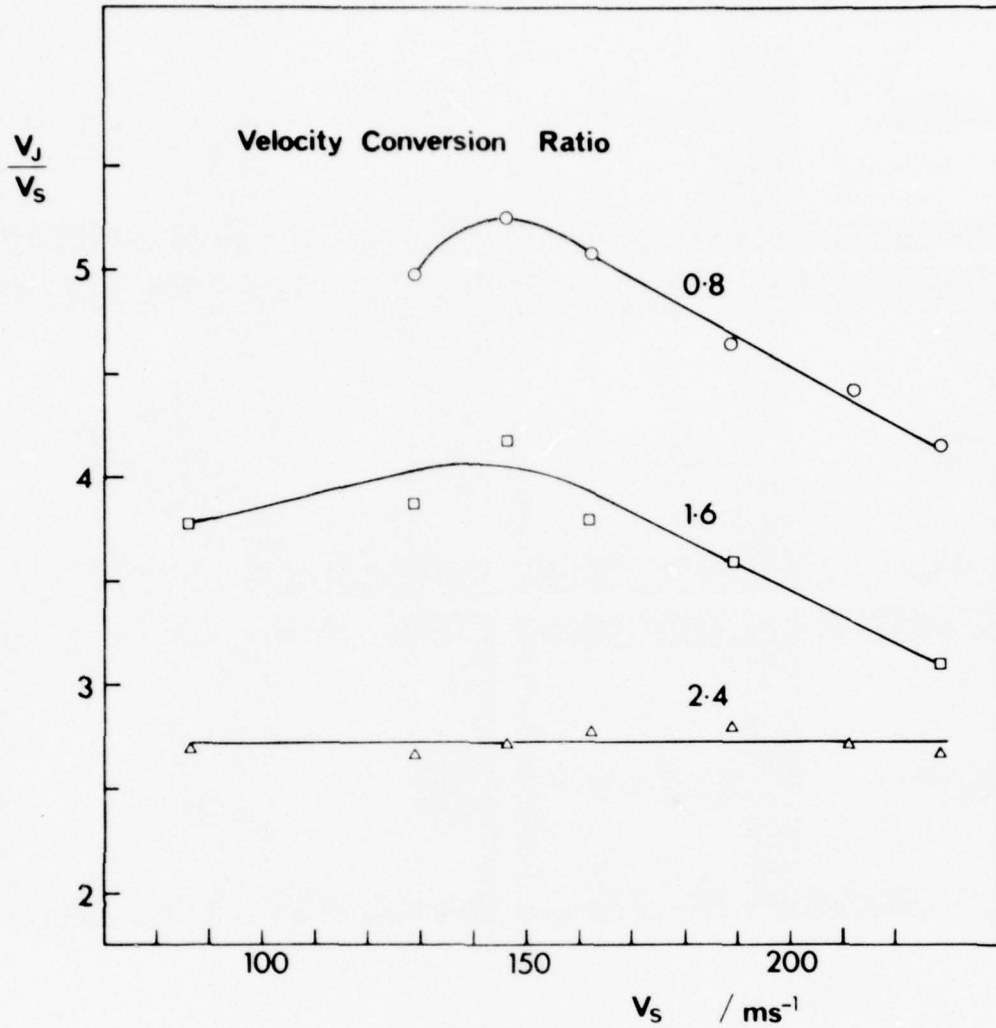


Fig 4

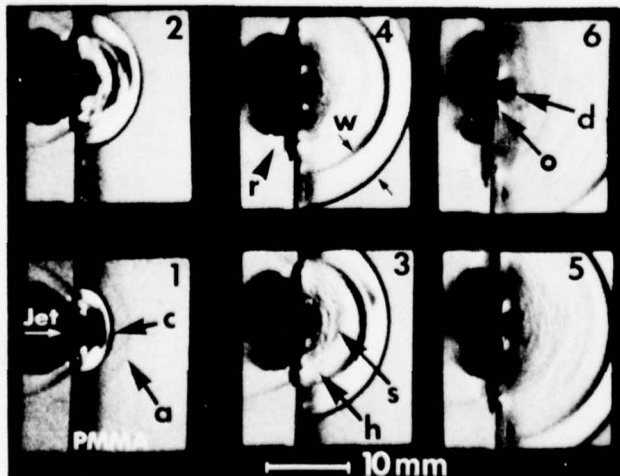


Fig 5

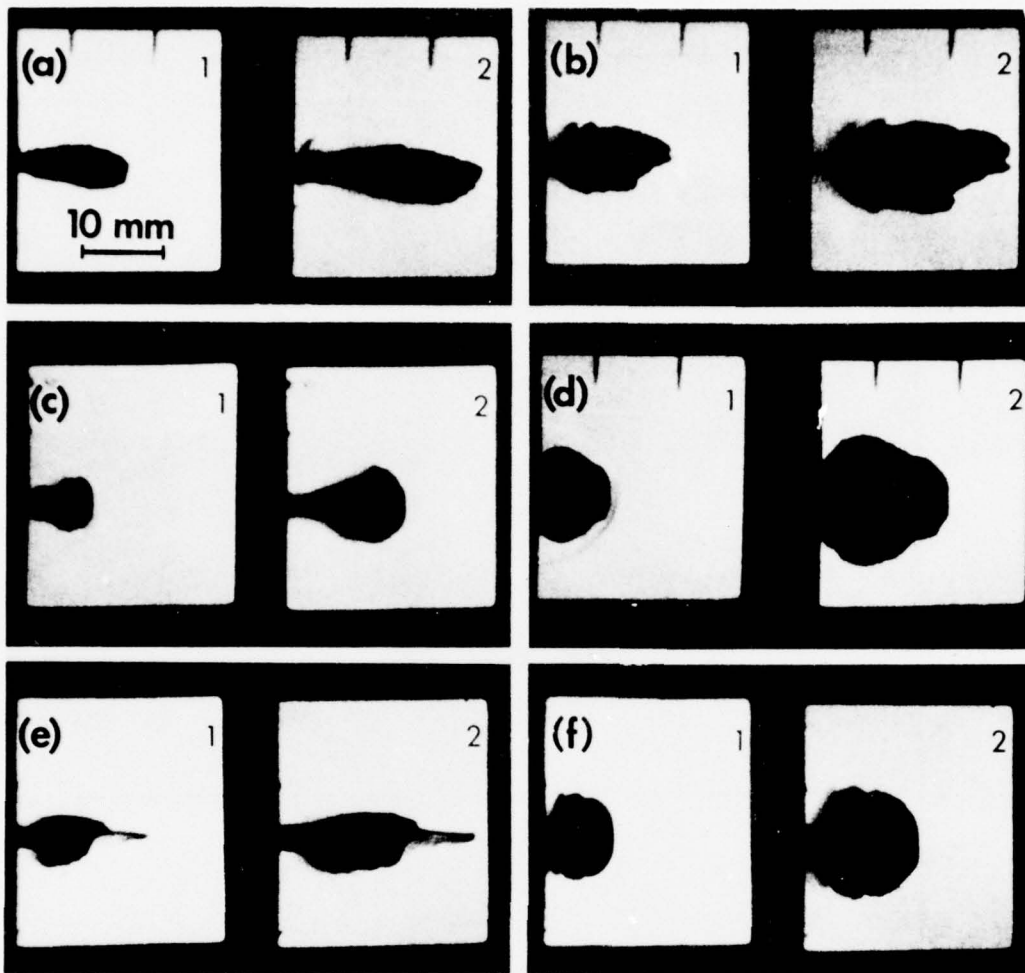


Fig 6

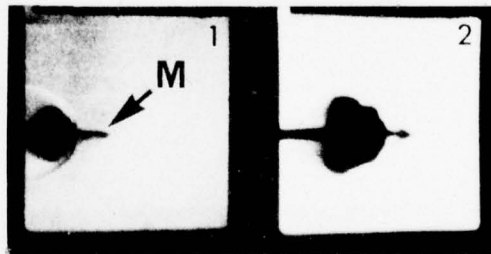


Fig 7

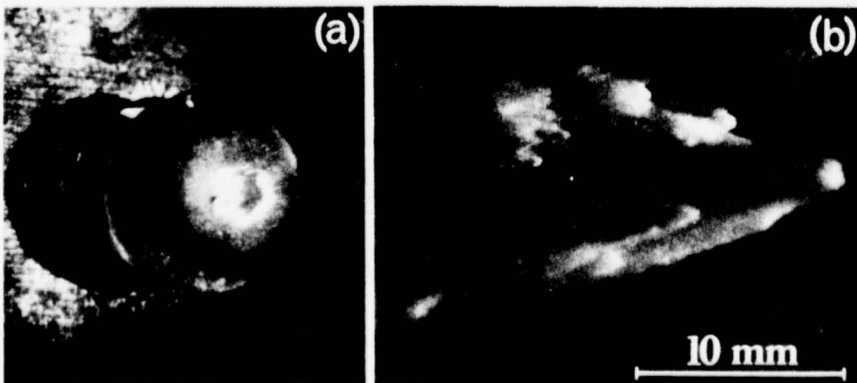


Fig 8

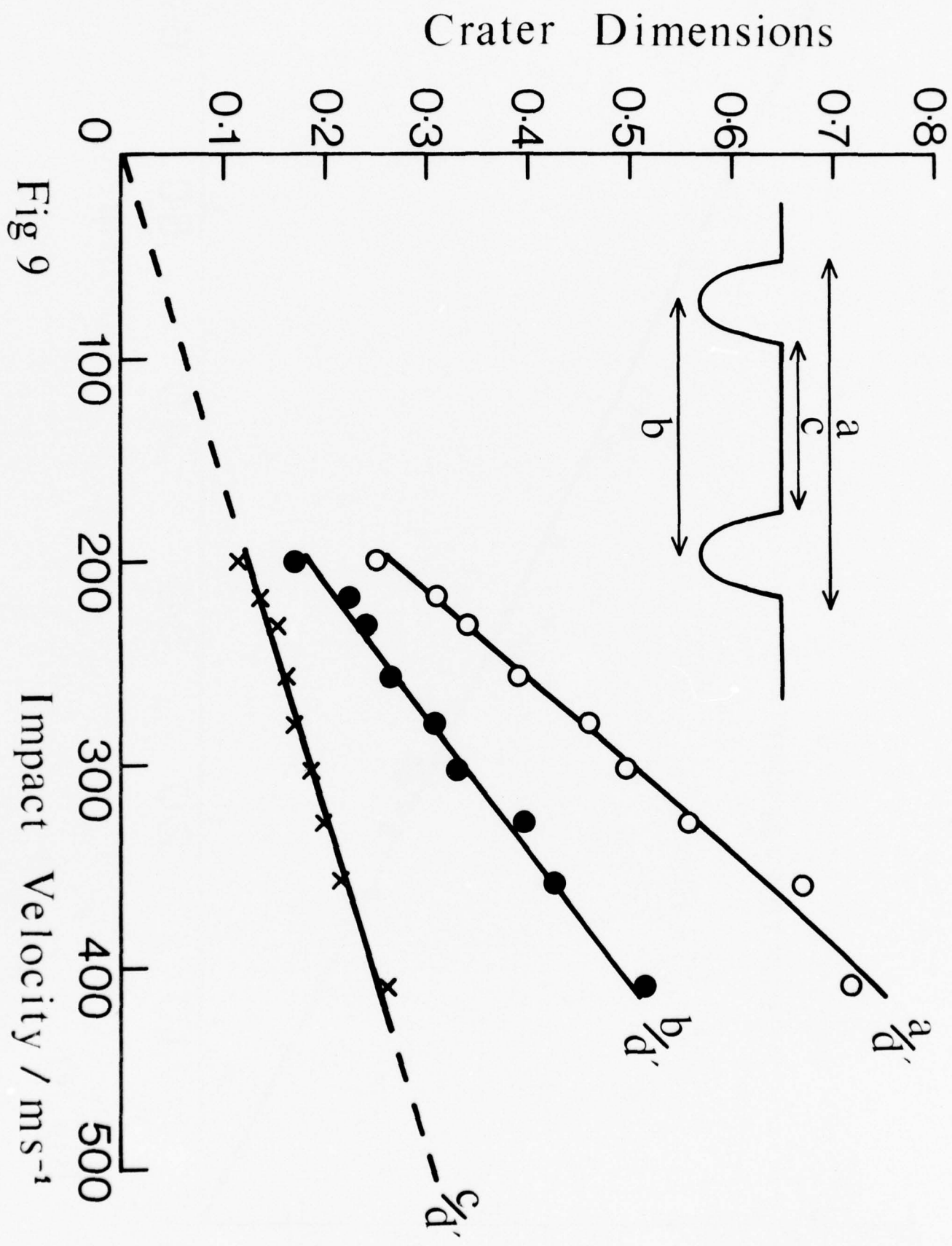


Fig 9

Impact Velocity /  $\text{ms}^{-1}$

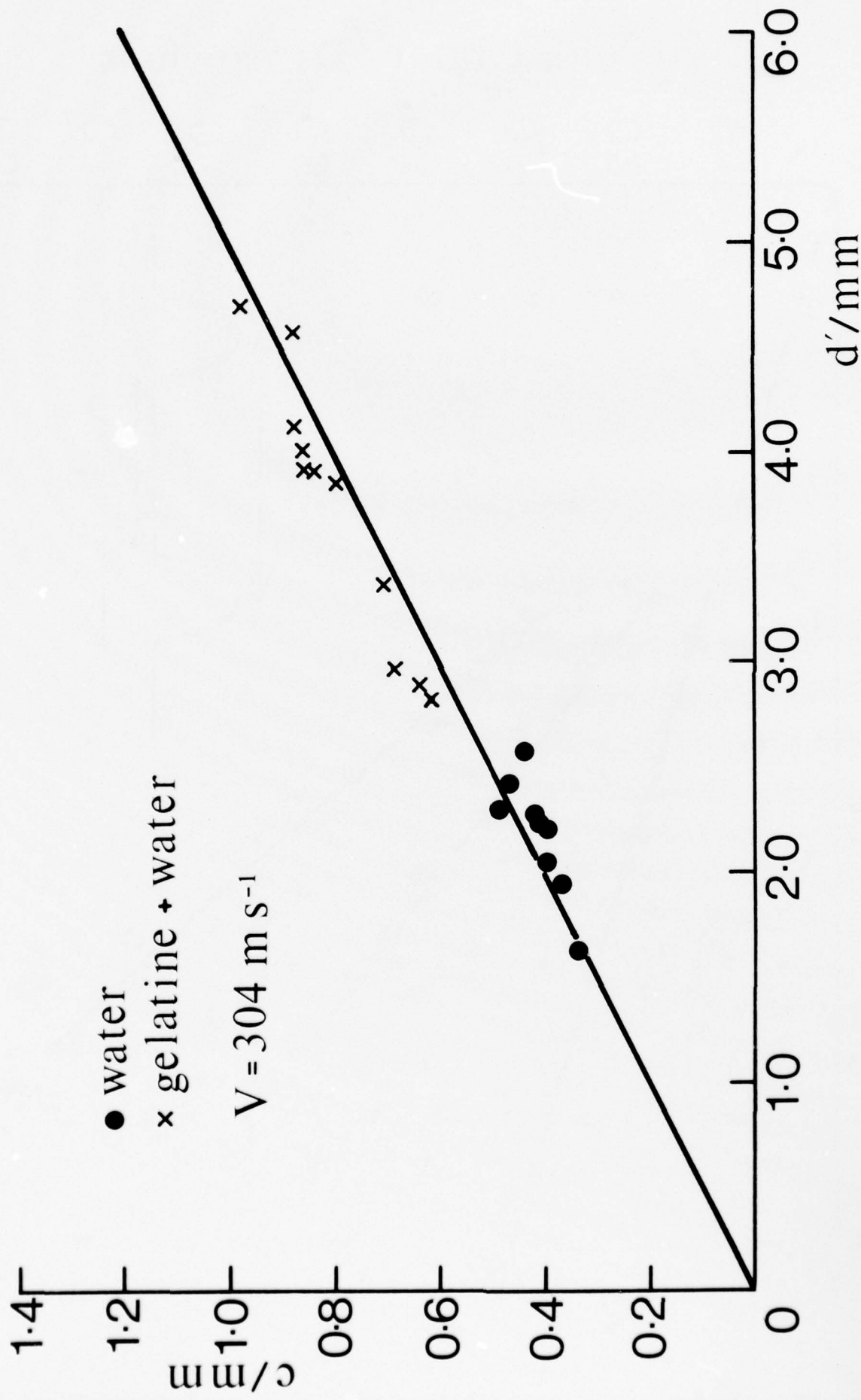


Fig 10

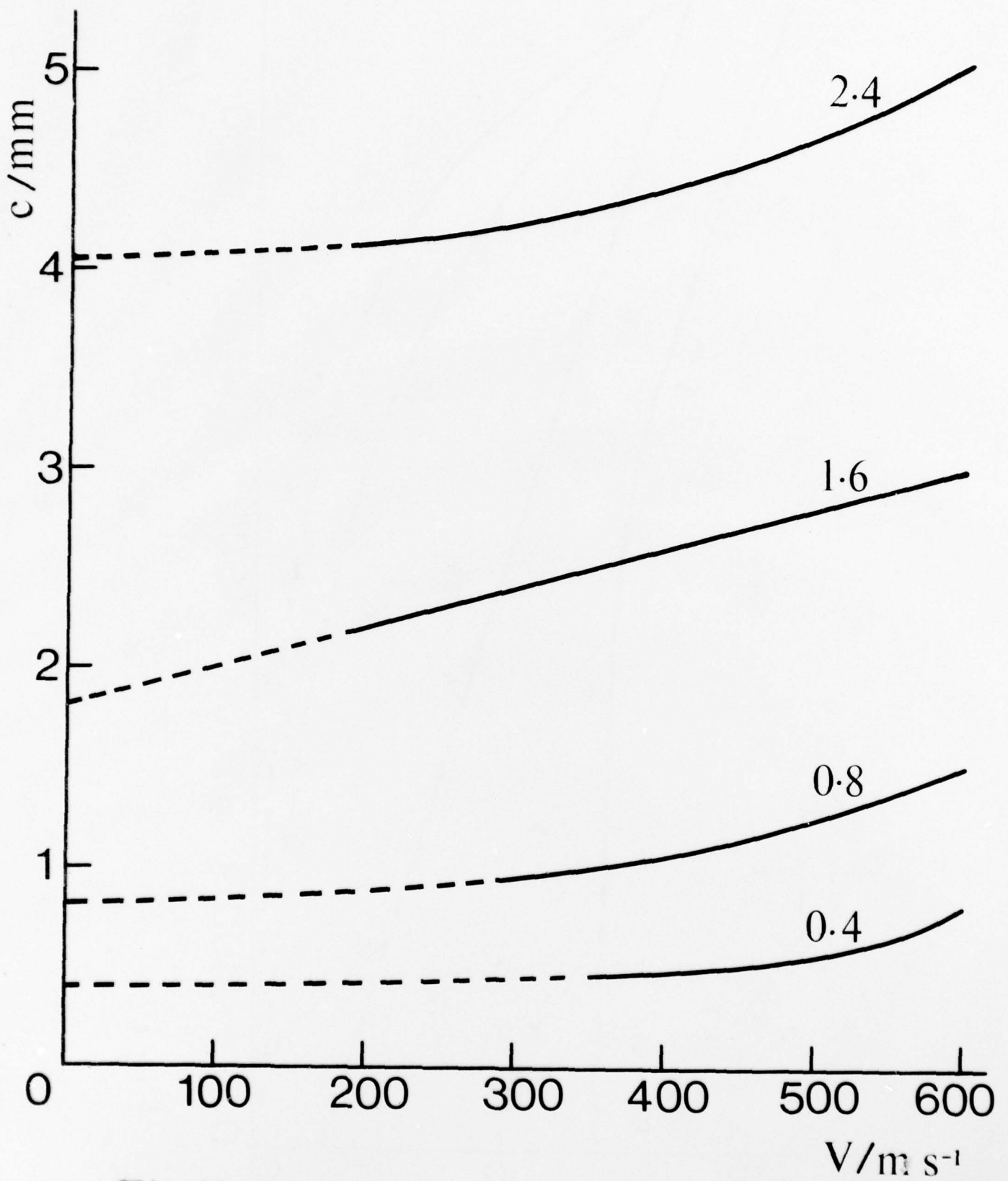


Fig 11

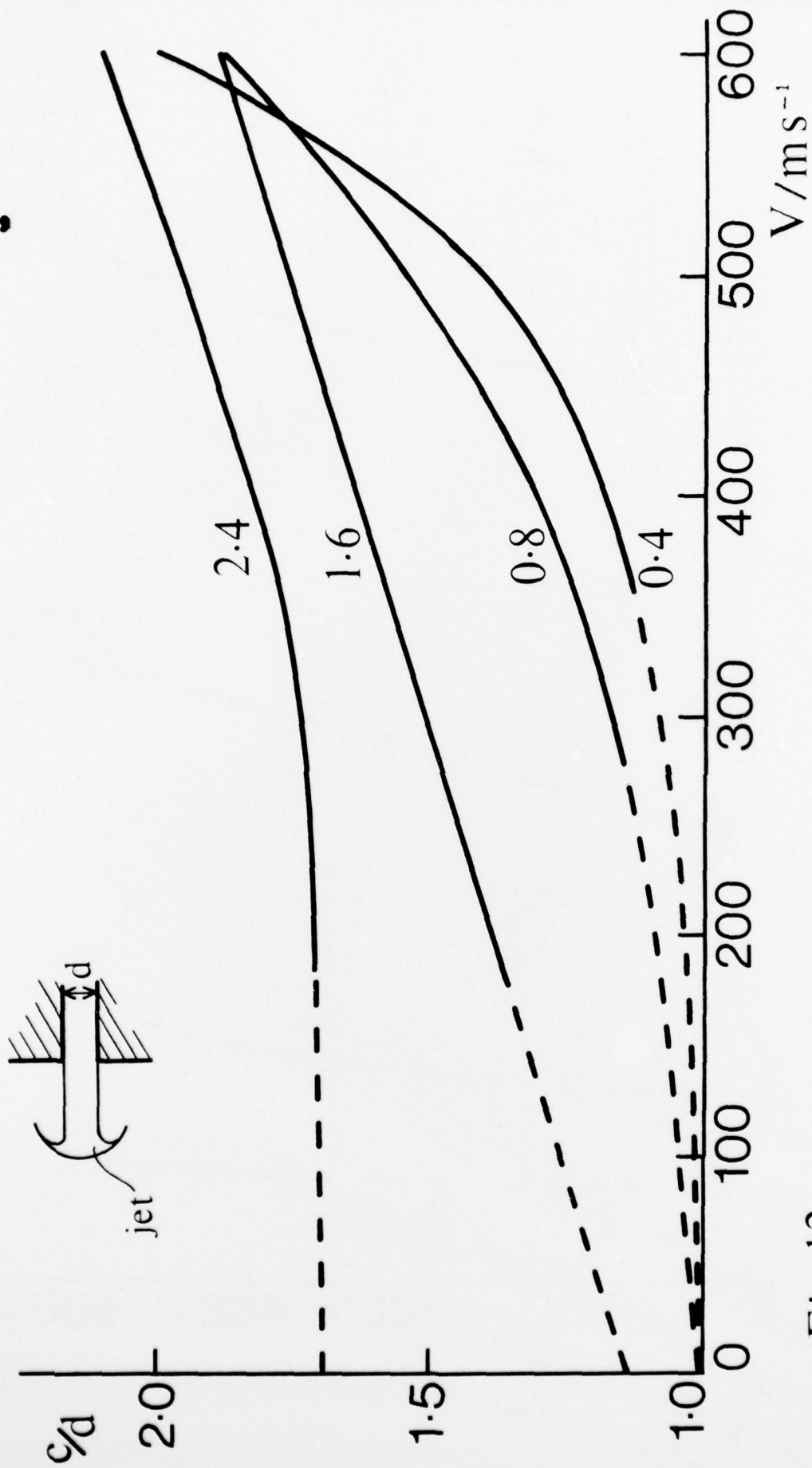


Fig 12

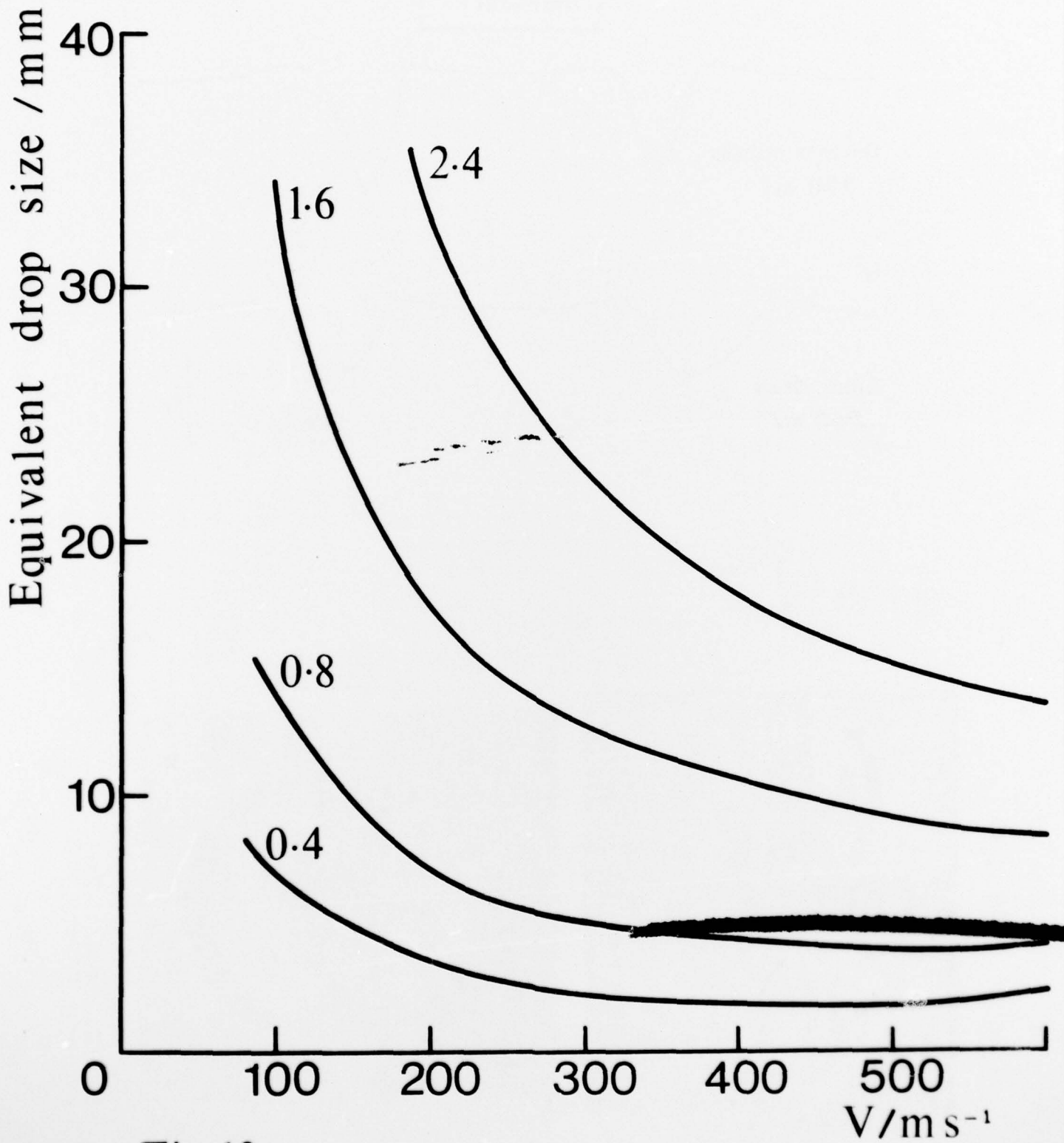


Fig 13

Fig 14

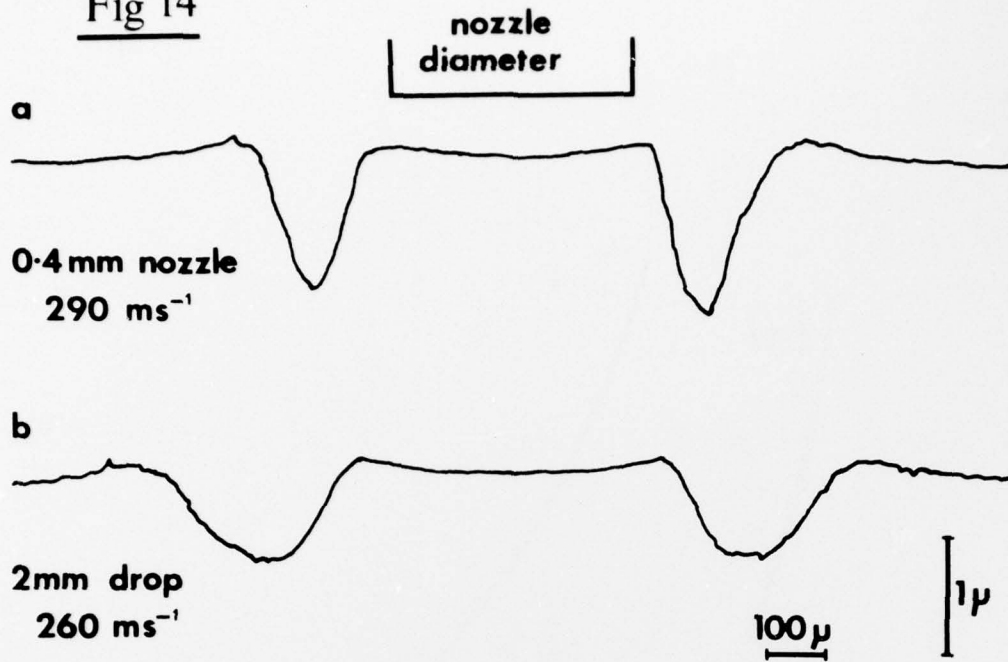
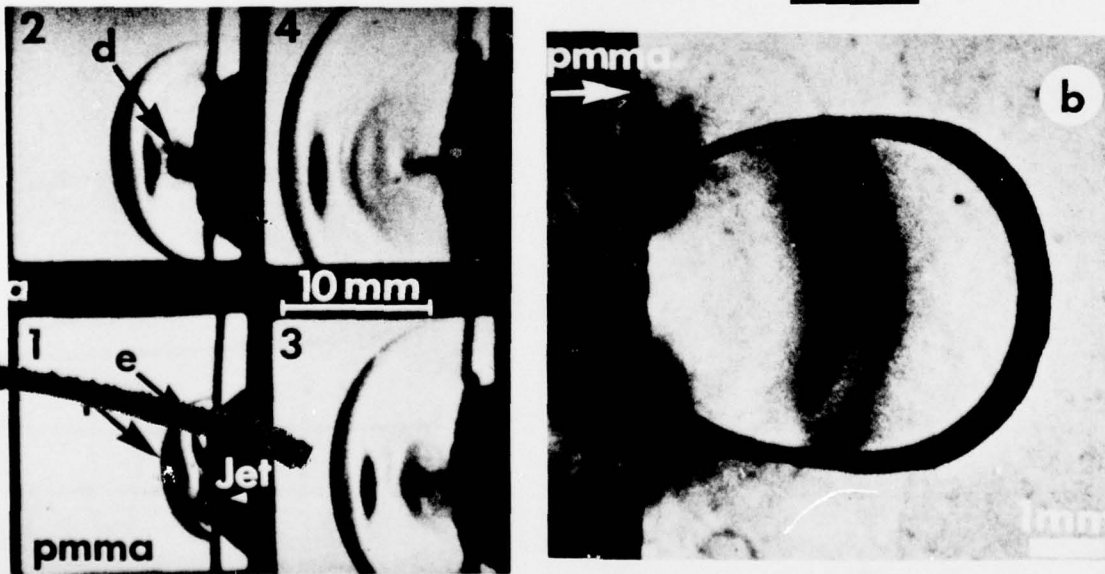
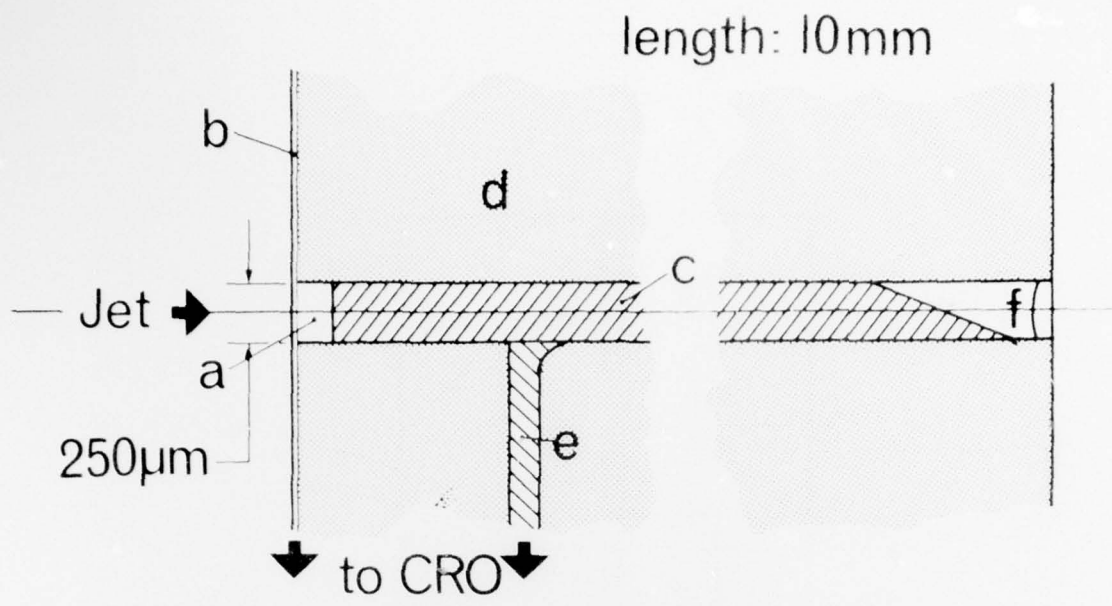


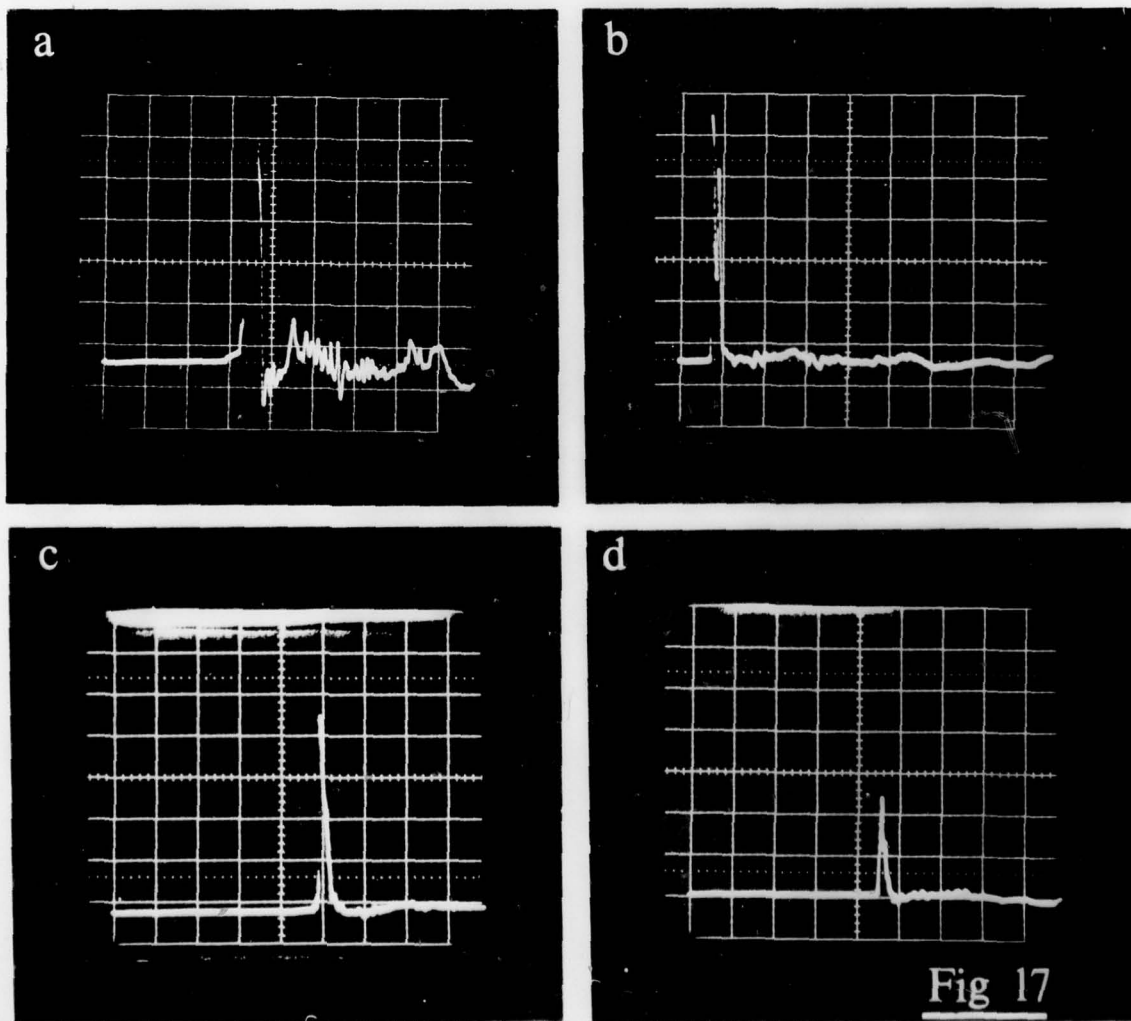
Fig 15





Pressure Transducer

Fig 16



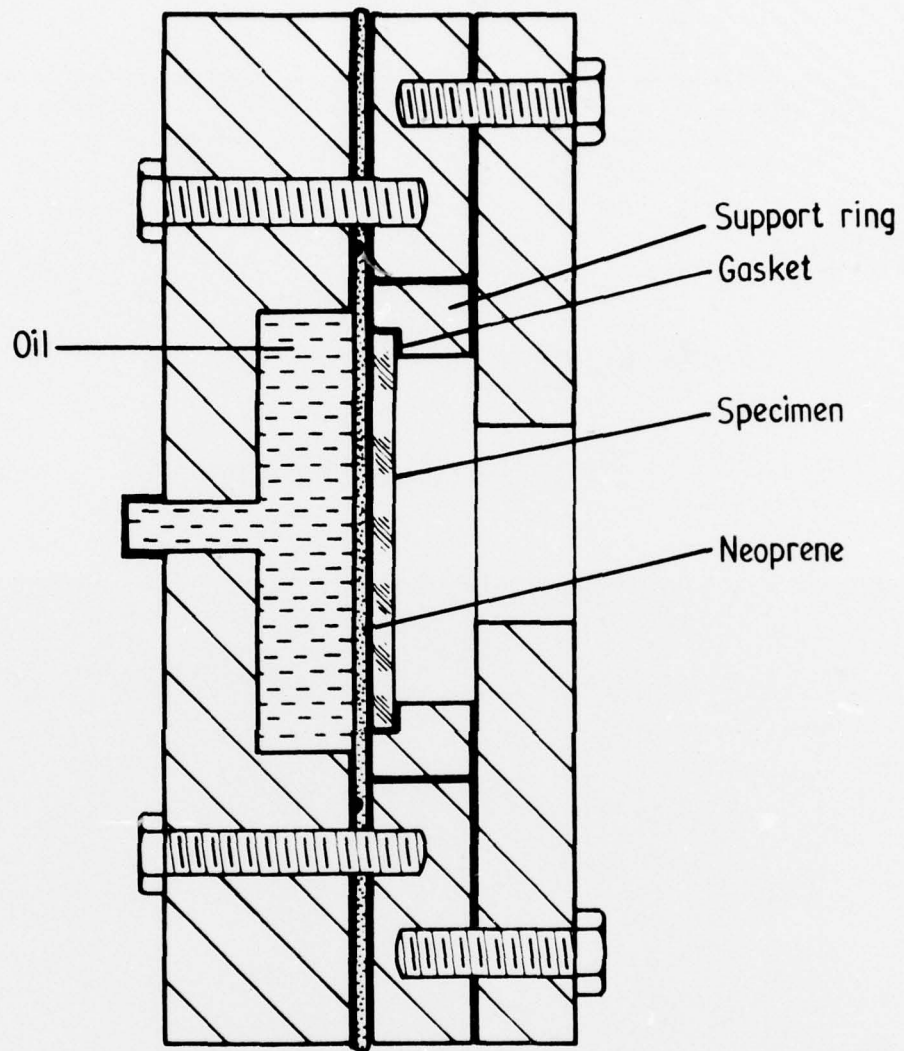


Fig 18

# Pressure Tester Calibration

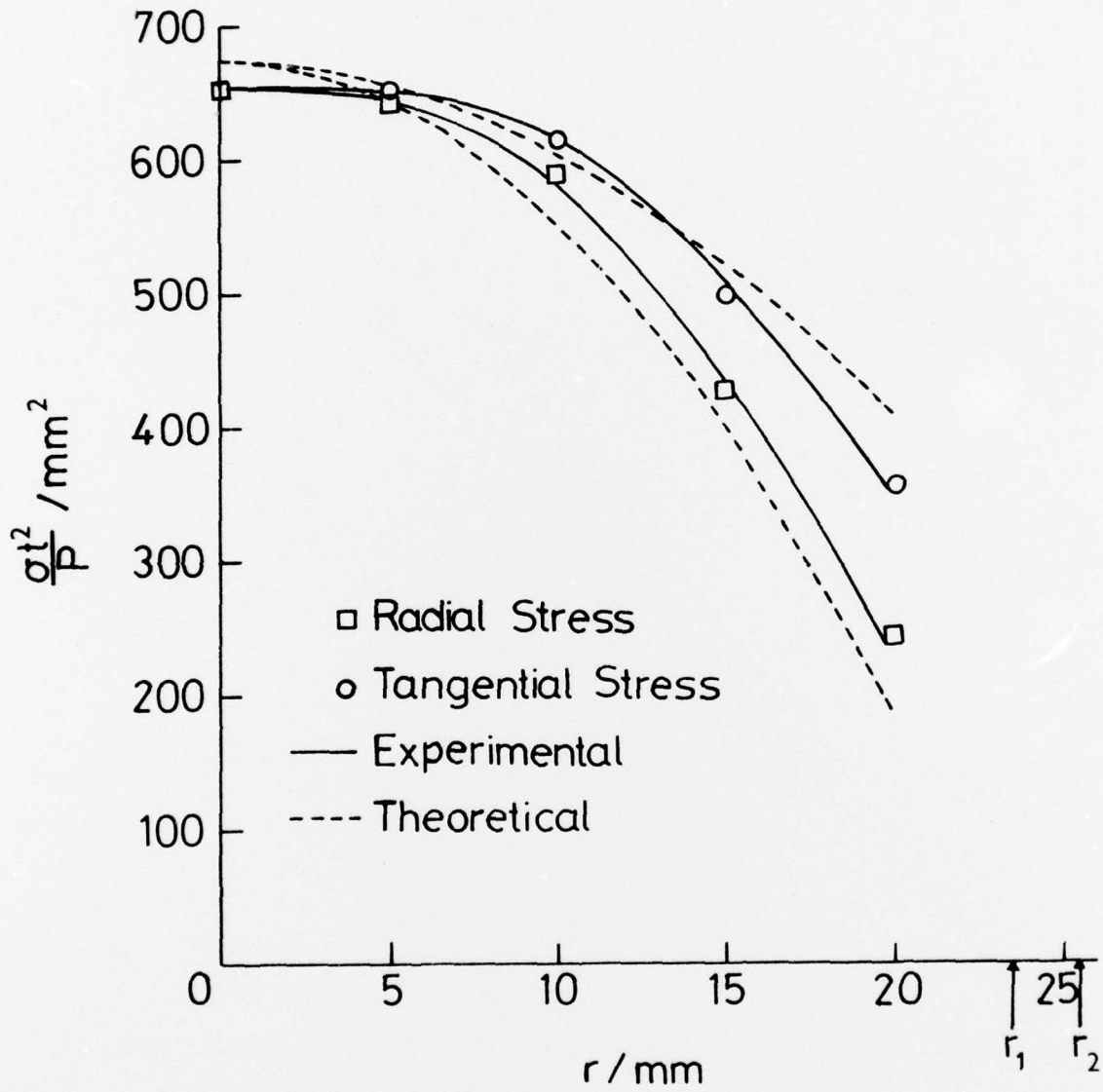


Fig 19

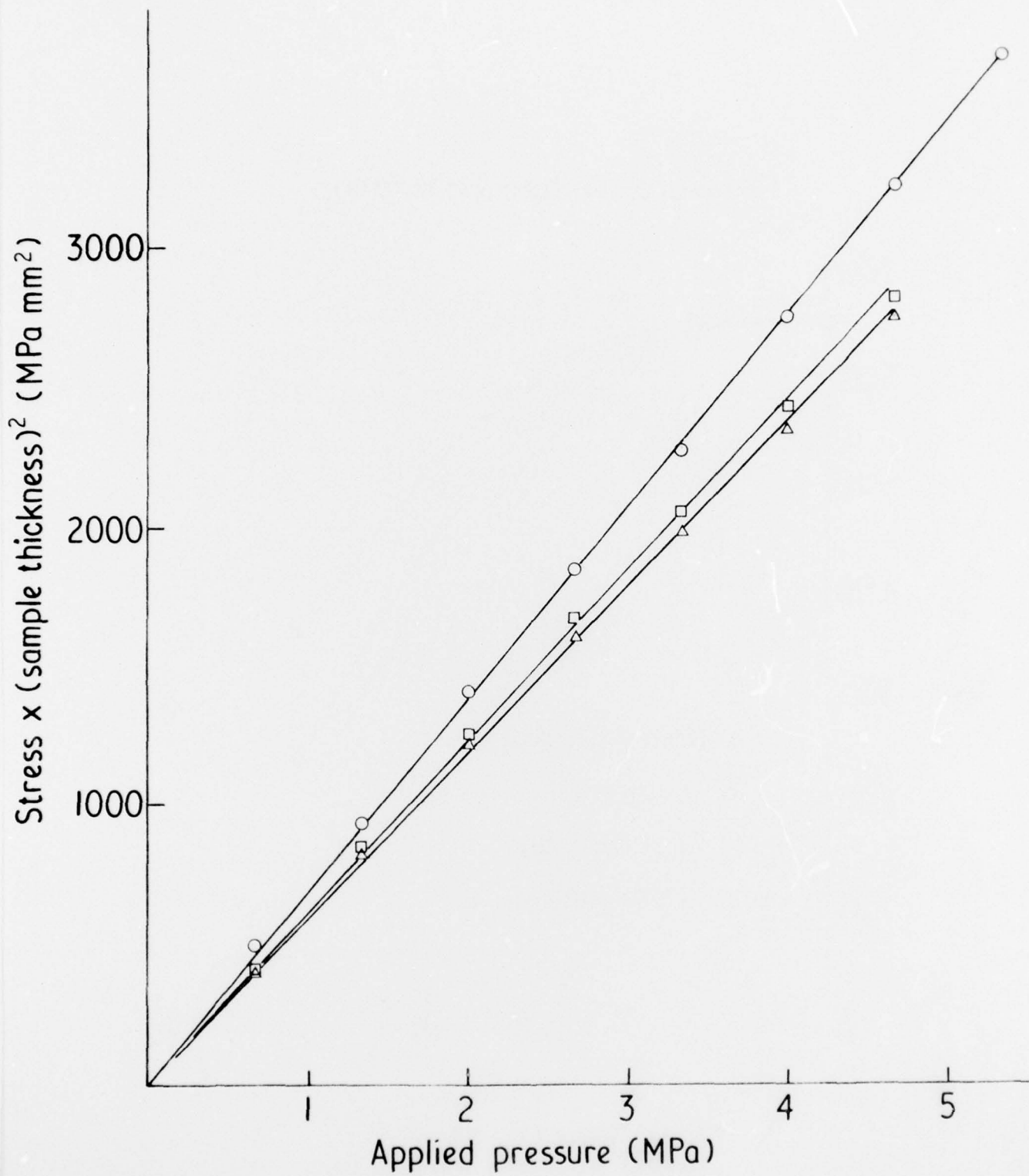


Fig 20

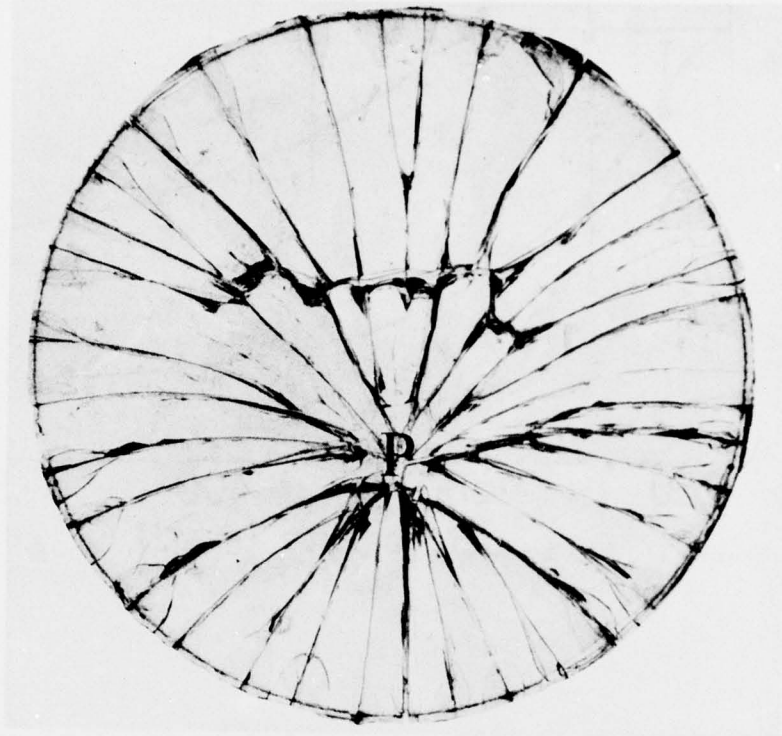


Fig 21

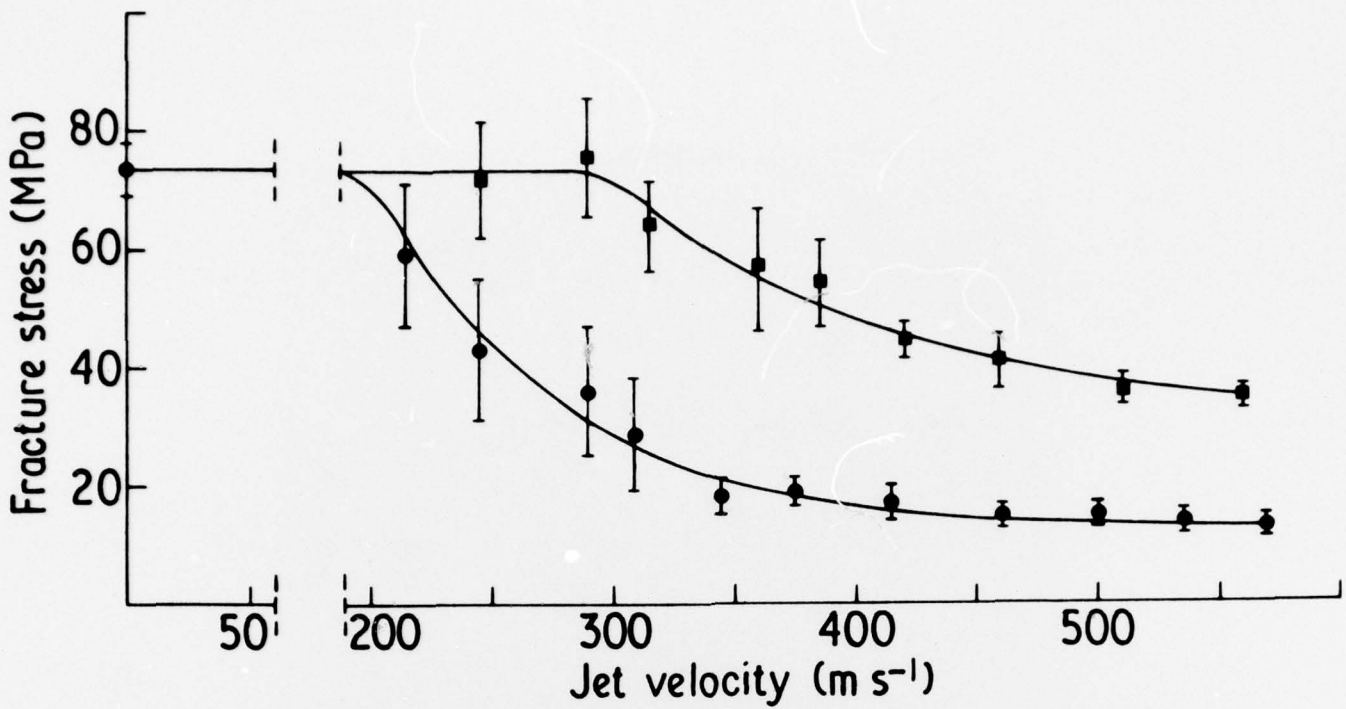


Fig 22

Residual Fracture Strength after Liquid Jet Impact (1.6mm nozzle)

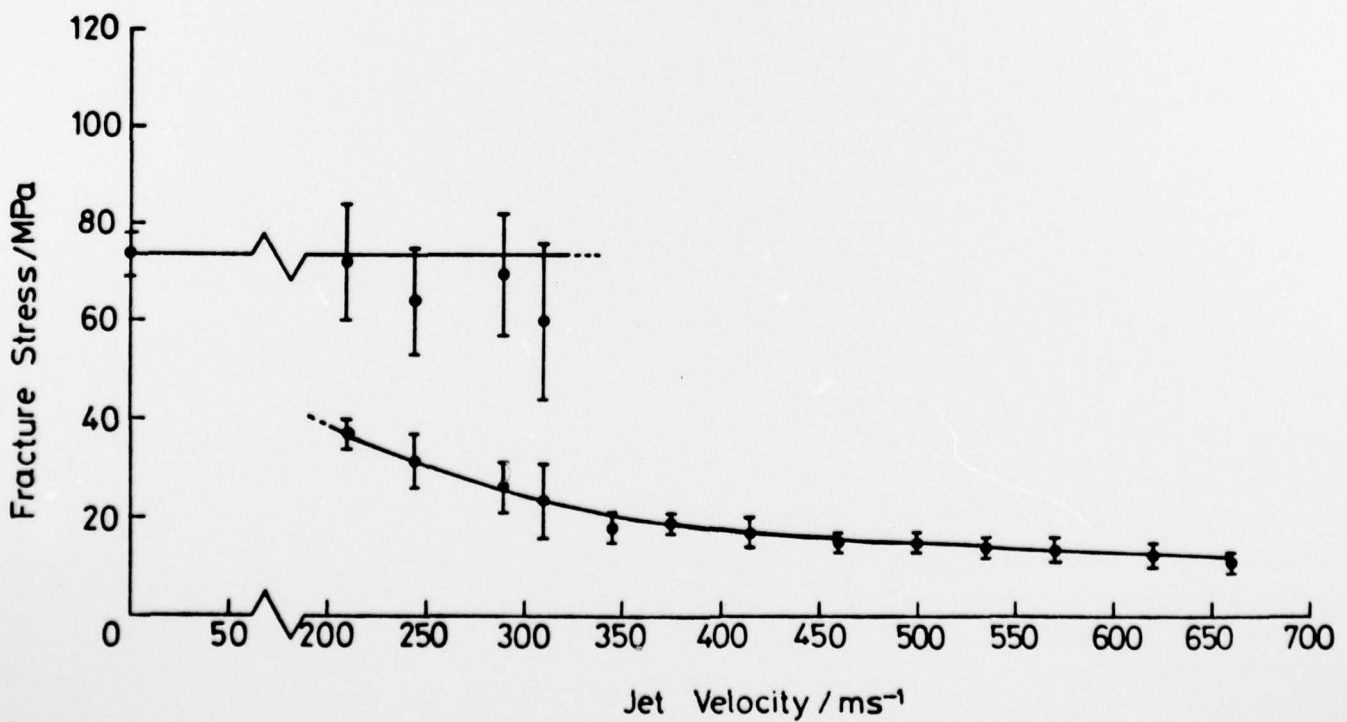


Fig 23

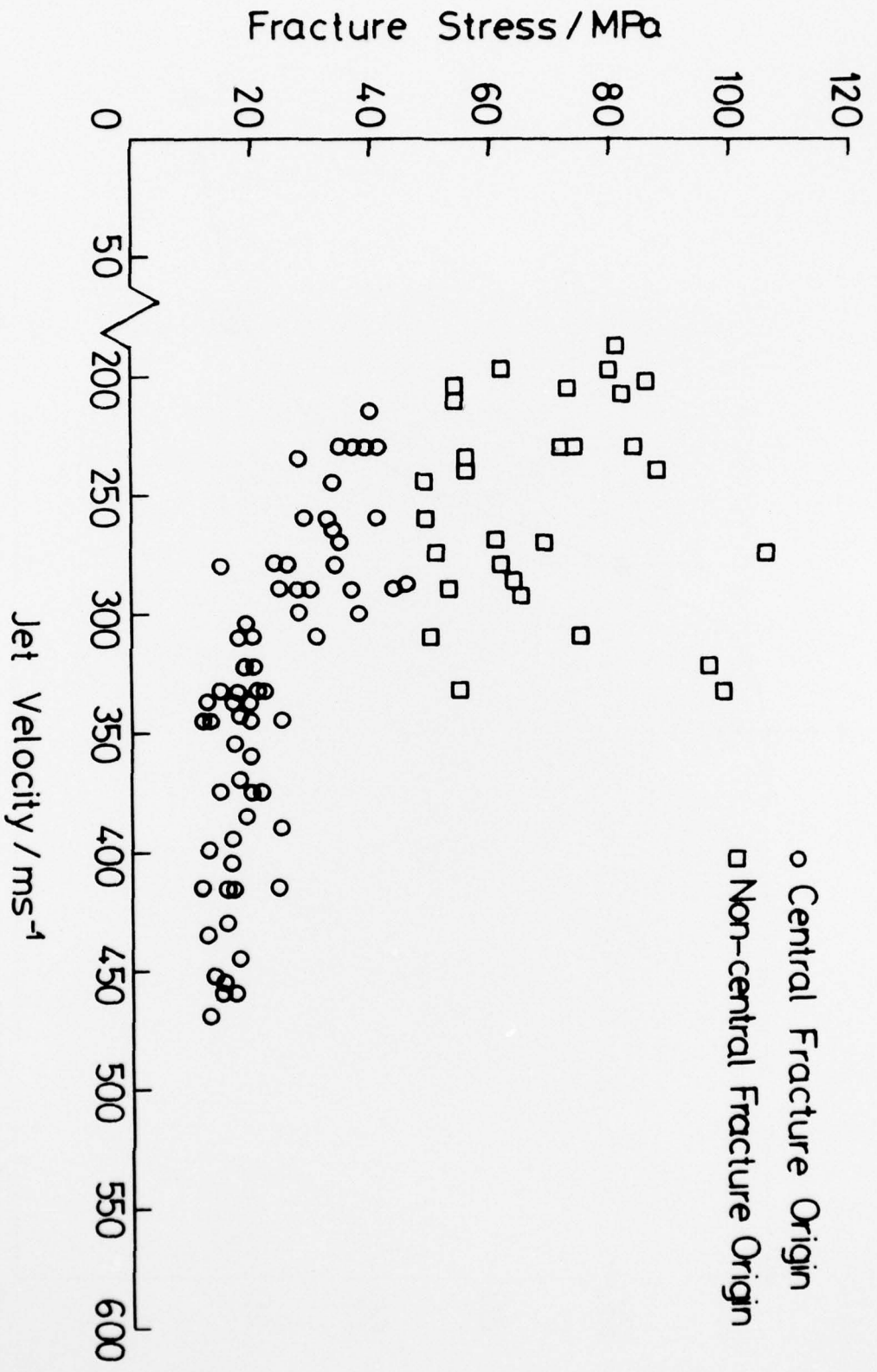


Fig 24

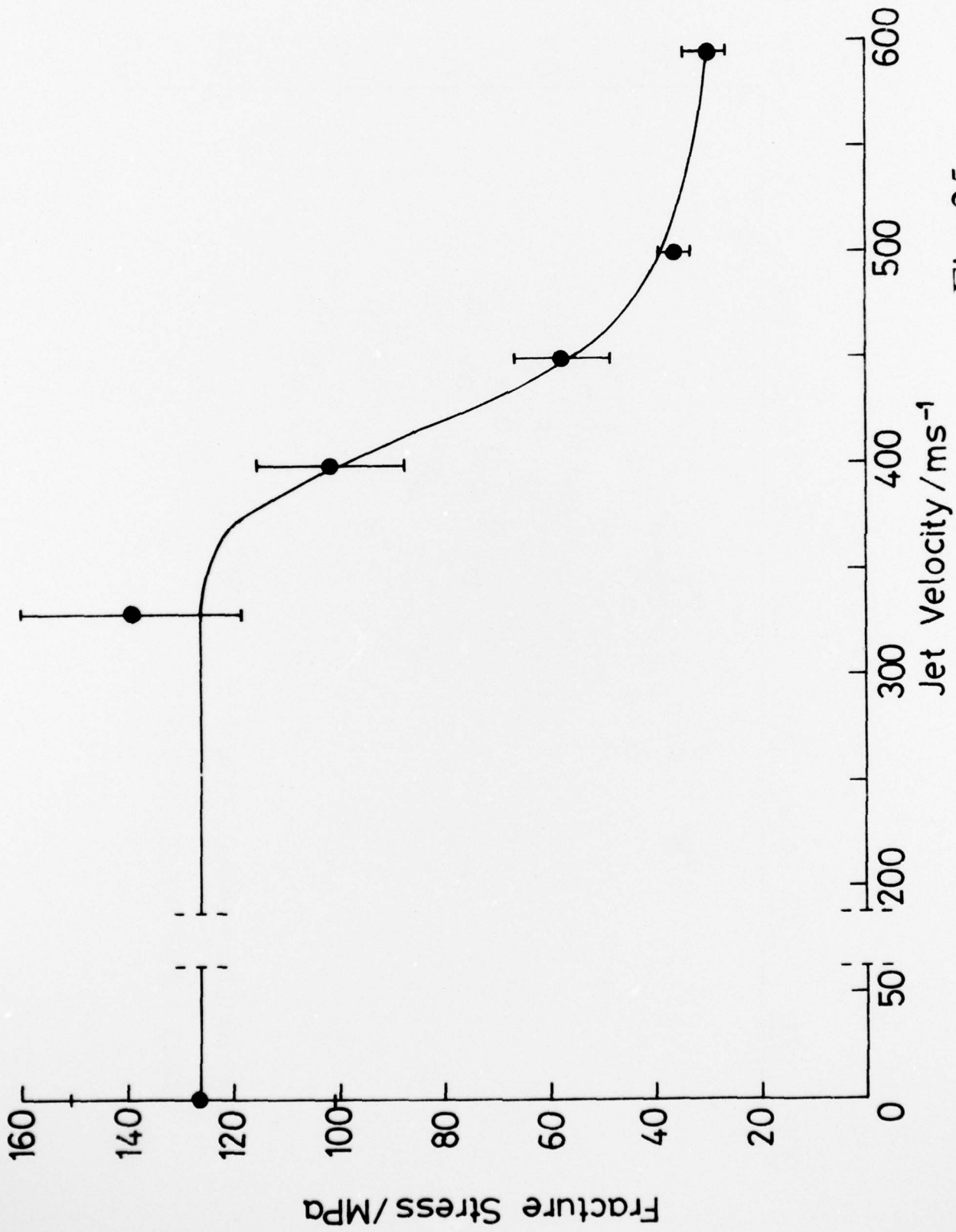


Fig 25

REPORT DOCUMENTATION PAGE

(Notes on completion overleaf)

Overall security classification of sheet .....UNCLASSIFIED.....

(As far as possible this sheet should contain only unclassified information. If it is necessary to enter classified information, the box concerned must be marked to indicate the classification eg (R),(C) or (S)).

1. DRIC Reference (if known)  BR-5507 ✓	2. Originator's Reference  DR Mat Report 203	3. Agency Reference	4. Report Security Classification  UNCLASSIFIED
5. Originator's Code (if known)	6. Originator (Corporate Author) Name and Location  Cavendish Laboratory ✓ University of Cambridge		
5a. Sponsoring Agency's Code (if known)	6a. Sponsoring Agency (Contract Authority) Name and Location  Director of Research, Materials MOD(PE), The Adelphi, London, WC2N 6BB		
7. Title High speed liquid impact studies.  A discussion of the apparatus and techniques used in studying liquid drop and jet impacts and assessing damage in a quantitative manner.			
7a. Title in Foreign Language (in the case of translations)  —			
7b. Presented at (for conference papers). Title, place and date of conference  —			
8. Author 1. Surname, initials  Field J E	9a. Author 2  Camus J-J	9b. Authors 3, 4...  Gorham D A Rickerby D G	10. Date 34 pp 30ret  December 1976
11. Contract Number  AT/2029/066 MAT	12. Period	13. Project	14. Other References
15. Distribution statement  UNLIMITED			
Descriptors (or keywords)  Impingement corrosion, Water impingement, Raindrops, Volume Hydraulic jets, Experimentation			
Abstract Two methods of producing high velocity liquid impact on solid targets are described. The jet method is described in full detail and the work aimed at relating jet impact damage to that produced by drop impact is fully discussed. High speed photography has been used extensively to study impact phenomena, and pressure measurements have been made using 250 µm diameter transducers. A hydrostatic test apparatus has been developed for measuring the "residual strength" of brittle specimens following impact. With glasses large strength losses can occur before the damage reaches visible dimensions. The factors affecting the residual strength curves are discussed.  Microimeters			

NOTES ON COMPLETION OF REPORT DOCUMENTATION PAGE

This Documentation Page is designed specifically for MOD reports and reports produced by Contractors.

Boxes marked\* below need be completed only if the information is readily available.

- \*1. DRIC reference: Enter DRIC reference (BR number) if one has been assigned.
2. Originator's Reference: Enter the report number by which the document is identified by the originator of the report, in the form in which it appears on the cover.
3. Agency reference: Enter reference number allocated by sponsoring agency (contract authority) in the case of contract reports.
4. Report Security Classification: Enter security classification or marking which limits the circulation of the report, or enter UNLIMITED when this applies.
- \*5. Originator's Code: Code number for the DRIC-standardised form of the entry appearing in Box 6.
- \*5a. Sponsoring Agency's Code: Code number for the DRIC-standardised form of the entry appearing in Box 6a.
6. Originator (corporate author): Enter name and location of the organisation preparing the report.
- 6a. Sponsoring Agency (Contract Authority): Enter the name of the monitoring MOD Branch or Establishment in the case of Contractor's reports. If an MOD report covers work funded by an outside agency, enter the name of that agency.
7. Title: Enter the complete report title in capital letters but omitting initial definite or indefinite articles. If the report covers a specific period, enter this after the title, eg (1.1.1972-31.3.1972).
- 7a. Title in Foreign Language: In the case of translations, enter the foreign language title (transliterated if necessary) and the translated English title in Box. 7.
- 7b. Conference Papers: If 7 is the title of a paper presented at a Conference, or a Conference proceedings, enter the Conference Title, where it was held and the date.
8. Author 1: Enter the name of the first author, followed by his initials.
- 9a. Author 2: Enter the name of the second author, followed by his initials.
- 9b. Authors 3,4...: Enter third and following authors' names.
10. Date: Enter the month (in figures) and the year of the report (Dec., 1969 is written 12.1969). If the report is undated but a period covered by the report is indicated, enter the date at the end of the period. pp.ref. Enter the inclusive number of pages in the report containing information, i.e. including appendices, tables and illustrations, and the total number of references cited.
11. Contract Number: Enter the number of the contract or grant under which the report was written.
12. Period: (always associated with the Contract Number). Only to be used for reports covering a specific period, e.g. quarterly, annual or final reports. Enter QR-1, AR, FR, as appropriate.
13. Project: Enter project name or number.
14. Other Reference: Enter any reference, other than those in Boxes 2 or 3, by which the report may be identified.
15. Distribution statement. Enter any limitations on the distribution of the document. If distribution is limited to particular groups eg MOD, MOD and its Contractors, etc. it should be stated. If the distribution is the responsibility of another authority eg a HQ Directorate (Technical Policy Authority) enter "Distribution controlled by MOD Technical Policy Authority". Enter "via DRIC" after "Authority" where appropriate and name the Technical Policy Authority if possible.

Descriptors: Any number of descriptors (or key-words) can be entered. If selected from a published thesaurus, eg The Thesaurus of Engineering and Scientific Terms (TEST), this should be indicated.

Abstract: The abstract should preferably not exceed 150 words, i.e. it can be considerably shorter than the Abstract to be provided on the Title Page of the Report. Information available in the report title need not be included in the abstract.